



Lebanese American University Repository (LAUR)

Post-print version/Author Accepted Manuscript

Publication metadata

Title: Direct Numerical Simulation of Transverse Ripples: 2. Self-Similarity, Bedform Coarsening, and Effect of Neighboring Structures.

Author(s): N. Zgheib, J. J. Fedele, D. C. J. D. Hoyal, M. M. Perillo, S. Balachandar

Journal: Journal of Geophysical Research: Earth Surface

DOI/Link: <https://doi.org/10.1002/2017JF004399>

"An edited version of this paper was published by AGU. Copyright (2018) American Geophysical Union."

How to cite this post-print from LAUR:

Zgheib, N., Fedele, J. J., Hoyal, D. C. J. D., Perillo, M. M., & Balachandar, S. (2018). Direct numerical simulation of transverse ripples: 2. Self-similarity, bedform coarsening, and effect of neighboring structures. *Journal of Geophysical Research: Earth Surface*, DOI, 10.1002/2017JF004399, <http://hdl.handle.net/10725/11523>

© Year 2018

This Open Access post-print is licensed under a Creative Commons Attribution-Non Commercial-No Derivatives (CC-BY-NC-ND 4.0)



This paper is posted at LAU Repository

For more information, please contact: archives@lau.edu.lb

DIRECT NUMERICAL SIMULATION OF TRANSVERSE RIPPLES

PART II. SELF-SIMILARITY, BEDFORM COARSENING, AND EFFECT OF NEIGHBOURING STRUCTURES

N. Zgheib^{1†}, J.J. Fedele², D.C.J.D Hoyal², M. M. Perillo², and S. Balachandar¹

¹*Department of Mechanical and Aerospace Engineering, University of Florida, Gainesville, FL 32611, USA*

²*ExxonMobil Upstream Research Company, Houston, TX 77098, USA*

Key points:

- Isolated ripples maintain a self-similar shape and bed shear stress profiles
- Bedform-bedform interactions can significantly modify bedform celerity
- Spectra of bed height variation suggest a Reynolds number dependence

Abstract

Coupled bed-flow direct numerical simulations investigating the early stages of pattern formation and bedform (ripple) interactions were examined in a previous paper (Part I), making use of the resolved flow field. In this paper (Part II), we compare our results to published experimental data and provide an extensive quantitative analysis of the bed using spectral analysis and two-point correlations. The effect of the mobile rippled bed on the flow structure as well as turbulence is investigated locally (at specific streamwise locations) as well as over the entire computational domain. We show that developing ripples attain a self-similar profile in both the shape and the corresponding bed shear stress. We demonstrate the importance of neighbouring structures, especially upstream neighbours, on bedform dynamics in terms of the growth, decay, and speed of ripples. Finally, we examine the defect-free interactions in the later stages of bed evolution, which primarily lead to wave coarsening.

[†] Address for correspondence: Department of Mechanical and Aerospace Engineering, University of Florida, Gainesville, FL 32611, USA

1. Introduction

In the companion paper ([Zgheib et al. 2017](#)), hereafter referred to as [Paper I](#), we examined the early stages of bed evolution and the reproducibility of the various stages of bed development, starting from a flattened bed. Using the near-bed flow field, we provided evidence on the role of locally intense vortical structures in initiating quasi-streamwise sediment streaks that evolve into incipient crestlines. Additionally, we investigated in detail the fluid mechanical origins of a number of defect-related bedform interactions and showed that for flow aligned interactions, the underlying mechanism is very similar, and that interactions are labelled differently depending on the geometry of interacting structures and the outcome of the interaction.

Substantial research over the past two decades has yielded a wealth of information on the spatial structure of mature ripples as well as their time evolution and interaction ([Ashley 1990](#), [Best 1992](#), [Ribberink & Al-Salem 1994](#), [Werner 1995, 1999, 2003](#), [Gyr & Schmid 1997](#), [Charru & Mouilleron-Arnould 2002](#), [Best & Kostaschuk 2002](#), [Coco & Murray 2007](#), [Howard 2007](#), [Ouriemi et al. 2009a,b](#), [Kocurek et al. 2010](#), [Swanson et al. 2016](#)). In this paper, we focus on the later stages of bed evolution in which ripples are found to attain a nearly self-similar, asymmetrical, triangular-like shape with a gentle slope on the stoss side and a steeper slope on the lee side corresponding to the angle of repose. At any instance during bed evolution, the size, and thus the speed, of bedforms may be different, which result in bedform interactions as smaller/faster ripples catch up to downstream larger/slower neighbours. Consequently, during the later stages of bed evolution, when the ripples span the entire width of the domain, these interactions primarily lead to wave coarsening. The coarsening process is fascinating and perhaps counterintuitively driven by the smaller upstream ripples starving their larger downstream neighbours ([Coleman & Melville 1994](#)). Additionally, we find that the coarsening process could be responsible in part for the relatively large scatter observed in experimental as well as numerical data pertaining to ripple speed and growth rate.

Similarly, there is a great body of literature on the mean flow and turbulence statistics over ripples and dunes. Significant emphasis in the past has been on investigating the simplified case of turbulent flow over fixed bedforms ([Nelson & Smith 1989](#), [McLean et al. 1994](#), [Bennett & Best 1995](#), [Kadota & Nezu 1999](#), [Venditti & Bennett 2000](#), [Zedler & Street 2001](#), [Balachandar et al. 2003](#), [Maddux et al. 2003](#), [Yue et al. 2005](#), [Coleman et al. 2006](#), [Grigoriadis et al. 2009](#), [Omidyeganeh & Piomelli 2013](#)). The resulting turbulence is statistically stationary and this assumption is justified on the basis that the evolution of the bed is on a timescale much longer than that of the turbulent flow. Furthermore, these investigations typically consider a fully developed ripple structure that has reached an equilibrium state. These studies focus on the main flow features such as the space and time-averaged flow field, flow separation on the lee side and size of recirculation region, as well as turbulent fluctuations at various streamwise positions. On the other hand, experimental or numerical studies showing the turbulence structure under mobile bed conditions ([Schindler & Robert 2005](#), [Coleman & Nikora 2011](#), [Hanmaiahgari & Balachandar 2016](#)) have been limited, but have yielded valuable information.

One of the methods for quantifying the structure and topology of bedforms is through the spectra of bed height variation ([Hino 1968](#), [Jain & Kennedy 1974](#), [Nikora et al. 1997](#)). In experiments, because of the difficulty in measuring bed elevation over the entire planform at the same time during a run, it is often the spectra of the equilibrium bedforms in the final stage of bedform evolution that is reported ([Perillo et al. 2014](#)). Alternatively, the instantaneous two-point correlation of bed height variation in numerical

simulations may be used to assess certain features including the stage of development of bedforms as well as the temporal rate of wave coarsening (Kidanemariam & Uhlmann 2014, 2017). Similarly, spatio-temporal correlations of bedforms are used to relate the speed to the size of the bedforms.

An interesting aspect of fully formed ripple and other bedform patterns is their self-similar nature (e.g. Andrle 1996, Coleman *et al.* 2006, Franklin & Charru 2009, Pelletier 2013). In the context of barchan dunes, Franklin & Charru (2009) found a self-similar shape of isolated dunes in both aeolian and subaqueous environments suggesting that their shape is independent of the transport mechanism. On the other hand, by conducting experiments on fixed two-dimensional dunes, Coleman *et al.* (2006) found that the flow in the near-bed region, specifically in the boundary layer, exhibits a self-similar profile. They argued that this near-bed, self-similar flow is central to the understanding of the feedback loop between the flow and underlying bed.

The purpose of this paper is to examine the self-similar state of fully-developed ripples and establish their statistical properties. Cross-sectional shape of the ripple, ripple height to wavelength ratio and ripple speed as a function of ripple height will be examined and compared with available experimental data. The self-similarity of the resulting flow field in terms of shear stress and recirculation region downstream of the ripple will also be examined. Direct numerical simulation results enable us to characterize the near-wall turbulence statistics as modified by the mobile bedforms and compare results against those established for fixed bedforms. The remainder of this paper is organised as follows. An examination of ripple properties from bedform spectra, Fourier expansions, two-point correlations, as well as turbulence and mean flow statistics is presented in §2 followed by a quantitative analysis of ripple self-similarity in §3. The process of wave coarsening and the inevitable scatter it introduces to wave speed and growth rate is discussed in §4. Discussion and conclusions are presented in §5 and §6, respectively.

2. Spectra, wave properties, and two-point correlation

2.1 Bedform spectra

Before we begin our discussion on bedform spectra, we would like to note that Tables 1 and 2 from paper I, which define many of the variables and provide details about the simulations are included in this part of the manuscript for completeness. The simulations considered in this section are for cases S1 through S6 of Table 2, those evolving from an initially flat surface. . The sediment bed height variation initially grows at an exponential rate (e.g. Jerolmack & Mohrig 2005, Fourriere *et al.* 2010, Kidanemariam & Uhlmann 2017) before approaching a plateau beyond the equilibrium stage of development. In Figure 1 we show the temporal evolution of the maximum (h_{max}) and rms (h_{rms}) values of the sediment bed height variation. Here, h_{max} and h_{rms} are defined as follows

$$h_{max}(t) = \max_{x,y}[h(x,y,t)] \quad ; \quad h_{rms}(t) = \sqrt{\frac{1}{L_x L_y} \int_0^{L_y} \int_0^{L_x} h^2 dx dy}, \quad (1)$$

where $h(x,y,t)$ is the bed height with reference to the initial flat bed, which remains as the mean bed height at all later time. The streamwise, spanwise, and vertical directions are denoted by x , y , and z , respectively. We remind the reader that all quantities have been nondimensionalized. The velocity scale

corresponds to the friction velocity U_τ^* defined in terms of the mean streamwise pressure gradient as $\rho_f^* U_\tau^{*2} / H_f^* = -\nabla^* p^*$, where the length scale H_f^* represents the mean flow depth. Here, and in the remainder of the paper, the asterisk denotes a dimensional quantity (similar to [paper I](#)). While h_{max} may locally attain values of about 8 to 15% of the mean flow depth, h_{rms} remains bounded to less than 5%. h_{rms} is a simple and common measure of surface roughness and is sometimes referred to as the interface width (e.g. [Barabási & Stanley 1995](#), [Jerolmack & Mohrig 2005](#)). We observe from [Figure 1](#) a strong dependence on the flow shear velocity. Cases [S1](#) through [S3](#), with the relatively higher U_τ^* value evolve faster than the relatively lower U_τ^* cases [S4](#) through [S6](#). This observation applies to both h_{max} and h_{rms} . We also observe a weak dependence of h_{max} on the grain size. Simulations with the smaller grain size (cases [S3](#) and [S6](#)) grow marginally faster than the corresponding larger grain simulations (cases [S1](#) and [S4](#)). However, this dependence is only observed for later times, $t_b \gtrsim 600$ and is not detected for h_{rms} . Here t_b represents non-dimensional time in bulk units ($t_b = t^* U_b / H_f$), and $U_b \approx 15.6 U_\tau$ is the initial bulk velocity obtained from the span and depth averaged flow field.

The initial exponential growth of h_{rms} can be observed in the log-linear plot of [Figure 1b](#), and the curve fits follow

$$h_{rms} = 10^{-3} \exp(0.015t_b) \quad \text{and} \quad h_{rms} = 4 \times 10^{-4} \exp(0.01t_b) \quad (2)$$

for the high and low shear stress cases, respectively. Thus the rate of increase in bed height variation for the higher shear stress cases is 50% larger than that for the lower shear stress cases. But the initial exponential growth only lasts for about $t_b \approx 150$ and $t_b \approx 250$ for the high and low shear stress cases, respectively. This is the period of formation of initial crestlines and their interaction and merger to form well-defined ripples. We should note that the exponential growth rate of 0.015 for the higher shear stress cases [S1](#) through [S3](#) is closer to the value of 0.014 observed by [Kidanemariam & Uhlmann \(2017\)](#) in comparison to the slower growth rate of 0.01 for the lower shear stress cases. Additionally, we find the duration of the exponential growth of bedforms for cases [S1](#) through [S3](#), which is about 200 bulk units to be very similar to that observed in [Kidanemariam & Uhlmann \(2017\)](#). The better agreement of the higher shear stress cases with the DNS results of [Kidanemariam & Uhlmann \(2017\)](#) is due to the fact that for cases [S1](#) through [S3](#), the ratio $\Theta/\Theta_{cr} \approx 4$ (See [Table 2](#)), is closer to the range of values used in [Kidanemariam & Uhlmann \(2017\)](#).

Subsequent evolution of the bed is at a much slower rate. During the initial period of this slower evolution the ripples continue to form and complete their evolution toward their approximate self-similar state. Even after they are fully formed, the ripples continue to interact through the merging and coarsening process. In terms of wall units, toward the end of the simulation, the rms bed height variation reaches about $h_{rms+} = 6.5$ and 8.0 for the high and low shear rate cases, and the corresponding peak ripple heights are about $h_{max+} = 14.5$ and 27, respectively. Thus, the ripples can be expected to substantially alter the nature of wall turbulence. We should note here that the ripple height (if interpreted as a roughness length scale) is in the hydraulically smooth regime (regarding the rms value), and at the lower end of the transitionally rough regime (regarding the maximum amplitude).

One of the methods for quantifying the structure and topology of bedforms is through the spectra of bed height variation. In experiments, because of the difficulty in measuring bed elevation over the entire planform at the same time during a run, it is often the spectra of the equilibrium bedforms in the final stage of bedform evolution that is reported. [Hino \(1968\)](#), [Jain & Kennedy \(1974\)](#), and [Nikora et al. \(1997\)](#)

have reported a -3 power decay for large wave numbers in the spectra of bed height variation. On the other hand, Kidanemariam & Uhlmann (2017) have reported a spectral power decay between -4.3 and -3.5 for their direct numerical simulations. The shear Reynolds number for which the -3 power decay was reported was in the range of $5 \times 10^3 < Re_\tau < 10^6$, which is more than an order of magnitude larger than $250 < Re_\tau < 350$ considered by Kidanemariam & Uhlmann (2017). In the present set of simulations for which $Re_\tau = 180$, we observe a decay rate of -3.75 (Figure 2), closer to the range reported by Kidanemariam & Uhlmann (2017). The spectra at four different times for case S2 are shown in Figure 2, and similar decay is observed for the other five cases. The larger spectral decay rate in the present study as well as in Kidanemariam & Uhlmann (2017) may suggest a Reynolds number dependence.

It can be observed that the spectra show an exponential decay at the very early time of $t_b = 5$. By $t_b = 98$, well-formed crestlines appear contributing to the power-law decay rate. The peak in the spectra at $k = 8$ corresponds to the emergence of about eight crestlines that occupy the streamwise extent of the computational domain. As the bed evolves, the spectra move up indicating temporal increase in the rms value of the bed height variation. Furthermore, the peak in the spectra moves from $k = 8$ to lower values indicating the coarsening of ripples. At $t_b = 500$, the peak is located at $k = 4$, and $t_b = 2381$, the peak is located at $k = 3$ indicating the dominance of four and three ripples at these times.

2.2 *Turbulence statistics and flow separation*

The patterns that form from the bed-flow interactions are not sinusoidal, but take a more triangular shape as shown in part 1 of the manuscript. In the following, we investigate the overall effect of a mobile rippled bed on the flow field. Figure 3 shows the rms velocity fluctuations for the streamwise, spanwise, and vertical components of velocity as well as the Reynolds stress versus distance from the bed for case S2. We consider two stages: (i) a completely flat bed (solid red line) and (ii) a mobile, rippled bed (black dashed and green dash-dotted lines). The first stage is representative of the start of the present simulations and corresponds to the classical pressure-driven open-channel turbulent flow over a smooth wall. Whereas the second corresponds to a pressure-driven open-channel turbulent flow over a complex, time-evolving rippled topology. The presence of the ripples contributes to macroscopic (large-scale) roughness induced form drag (Einstein & Barbarossa 1952, Engulend 1977, Fedele & Garcia 2001). As a result, when the bed was completely flat (at $t_b = 0$), the streamwise pressure gradient was entirely balanced by skin friction along the bed. At later times, the pressure gradient is partly balanced by skin friction and partly by form drag. Thus in the present simulations where the driving mean pressure gradient was held fixed (Re_τ is a constant), the formation of bedforms results in a lowering of the mean shear stress. At the start of the simulation at $t_b = 0$ when the bed is still completely flat, the local streamwise, spanwise and bed-normal directions (in the frame of reference of the bed) coincide with the x , y , and z directions, respectively. However, as the shear stress is allowed to work and modify the bed, the bed-tangent and bed-normal directions will no longer be necessarily aligned with the horizontal and vertical directions. To that end, we present the data for $t_b > 1000$ in Figure 3 in two coordinate frames. We should note here that this analysis is done in post-processing with a simple change of coordinate system. The first coordinate frame is aligned with the computational domain such that the streamwise, spanwise and vertical components of velocity are along the x , y , and z directions, respectively, irrespective of the shape of the bed. Whereas

in the second coordinate frame, the alignment of these velocity components is with respect to the bed. The former coordinate frame is more appropriate away from the bed, where the direct effect of the ripples on the flow is relatively weak and the streamlines are predominantly aligned with the x -direction. On the other hand, the bed-based coordinate frame is more appropriate in the near-bed region where the streamlines are strongly dependent on the shape of the bed. These two coordinate frames are denoted by z_v and z_n for the former and the latter, respectively. Note that in both coordinate frames, the fluid/sediment interface corresponds to $z_v = 0$ and $z_n = 0$ (recall that both coordinate frames extend from the bed outward). The peak Reynolds shear stress for the flat bottom boundary (red curve in frame d) occurs at around 30 wall units above the bed in the buffer region, well above the viscous sublayer. The location of the peak is slightly lower (black dash curve) in the case of the rippled bed and this is consistent with the reduction in the mean wall shear stress, as part of the pressure gradient is balanced by form drag.

We observe the streamwise and spanwise velocity fluctuations ($u_{x\text{rms}}$ and $u_{y\text{rms}}$) to be weakly dependent on the choice of coordinate frame. Alternatively, $u_{z\text{rms}}$ (frame c) and the Reynolds stress (frame d) exhibit a significant difference between the two coordinate frames showing the importance of choosing the correct description of bed-normal distance in the near-bed and far field regions. For example, the Reynolds stress in [Figure 3d](#), when computed in the computational coordinate frame, initially attains a negative value near the bed, before changing signs and attaining positive values at around $z \approx 0.08$. However, when the bed-normal coordinate frame is employed, the results are qualitatively and quantitatively different. We do not observe qualitative differences in the profile of the velocity fluctuations or the Reynolds stress due to the presence of the ripples. We do however observe the velocity fluctuations to increase near the bed. This near-bed rise in the rms velocity values comes at the expense of the mean flow which is constrained by the presence of the ripples and consequently reduced over time as seen in [Figure 4](#). It should be noted that in the bed-normal coordinate system, the plot of $u_{z\text{rms}}$ remains a constant with increasing z_n and this is due to the fact that, away from the bed, a component of the streamwise velocity fluctuation appears as the bed-normal component. Thus, the optimal coordinate appears to be one that is normal to the bed in the near bed region and turns to the vertical direction sufficiently far away.

It is important to understand how the mean velocity profile is affected by the presence of bedforms. [Figure 4](#) shows the vertical z -profile of the stream and span-averaged x -component of the flow at different time instances for case S2. We take the position of the bed into consideration by using the z_v coordinate. Recall that $z_v = z - h(x, y, t)$ represents the vertical distance from the bed. The red solid line corresponds to the velocity profile at the start of the simulation when the bed is completely flat. Two other time instances are considered, namely $t_b = 500$ (purple dash-dotted line) and $t_b = 2381$ (black dashed line). The inset of [Figure 4](#) shows a log-linear plot of \bar{u}_τ in wall units ($z_v^+ = z_v^* \bar{u}_\tau^* / v^*$) for the same time instances (note that the axes are flipped between the main figure and the inset). The thick solid black line corresponds to $\bar{u}_\tau = z_v^+$ and conforms to the velocity profile in the viscous sublayer. Note that z_v^+ and z^+ are identical at the start of the simulation as the bed is completely flat. The blue triangular and red circular symbols in the inset correspond to results from a rough wall, open channel flow, fully-resolved direct numerical simulation ([Chan-Braun et al. 2011](#)). The geometrically rough wall in the simulations of Chan-Braun et al. (2011) consisted of a layer of spheres in a square arrangement. Two arrangements were considered. The first case (blue triangles in [Figure 4](#)) had small spheres whose diameter is equivalent to 10.7 wall units, whereas for the second case (red circles) the spheres were larger with an equivalent diameter of 49.3 wall units. The Reynolds number of the flow, based on bulk velocity, was around $Re_b \approx 2900$, which is

comparable to the bulk Reynolds number of our simulations ($Re_b \approx 2800$). As expected, we find that as the bedforms grow in amplitude, their effect on the flow is similar to the effect of an actual rough wall, with increasing roughness. At $t_b = 500$, the bedforms are still relatively small and we observe the velocity profile (dash-dotted line) to be closer to the profile of the flow over an actual rough wall (blue triangles). On the other hand, we find that when the bedforms are nearly fully developed (dashed line), the velocity profile shifts further away from the profile over a smooth wall.

At the start of the simulation, we find the logarithmic-law profile as shown in (3) to properly describe the velocity profile in the outer region when B takes on the standard value of 5.1 (Nikora *et al.* 2001, Jimenez 2004). The logarithmic-law profile is given by

$$\bar{u}_x = \frac{1}{\kappa} \ln(z_v^+) + B, \quad (3)$$

where $\kappa \approx 0.41$ is the universal von Kàrmàn constant and B is a constant that depends on the roughness of the bottom surface. As the bed evolves and the large-scale/macrosopic roughness of the sediment bed increases, B takes on smaller values of 4.1 (solid orange line) and 1.2 (solid cyan line) at $t_b = 500$ and 2381, respectively (see Figure 5a). We should note here that the thickness of the layer pertaining to the logarithmic-law profile at those two instances is significantly reduced (overlap region between computed velocity profile and logarithmic-law profile) and thus the flow has become barely turbulent (e.g. Spalart 1988). In fact, by inspecting the velocity profiles for the entire duration of all six simulations in Table 2, we find the coefficient B to follow a similar trend for open channel flows with small scale roughness (Nikuradse 1933) as seen in Figure 5b where B is plotted as a function of the rms bed height variation in wall units, h_{0rms}^+ ($h_{0rms}^+ = h_{rms}^* U_\tau^* / \nu^*$). B shows a monotonically decreasing trend with h_{0rms}^+ starting from $h_{0rms}^+ = 0$ (initial flat bed). This decreasing trend is due to the reduced flow rate over the rippled bed (as compared with the flow rate over the initially flat bed) as a result of the emergence of bedforms coupled with the constant mean pressure gradient that is applied along the flow direction.

As the cross-sectional area of the flow varies substantially along the streamwise direction due to the presence of the rippled bed, the resistance to the flow increases, and the volumetric flow rate Q of the overlying fluid decreases over time as seen in Figure 6a. In fact, the flow rate decreases because a constant streamwise pressure gradient is maintained while the increasing bedform amplitude offers increased resistance to the flow. As mentioned previously, had the flow rate been maintained constant and the top surface allowed to evolve, then this scenario would have been different. Here the flow rate is normalized by the flow rate Q_0 over the initially flattened bed. The decrease is more rapid in the high shear cases S1-S3, and the flow rate in the presence of the mature ripples appears to settle to a new equilibrium value of about 65% of the initial value for a flat bed. As the flow rate decreases, so does the total shear stress on the bed (Figure 6b). Because of the imposed constant pressure gradient in the streamwise direction, the increase in form drag accounts for the drop in shear stress. Here again we observe the mean shear stress to reach a stationary state in the higher shear cases S1-S3. Additionally, we find the mean shear stress in the presence of the ripples to be around 40% of the initial average shear stress over a flat bed.

In the very early stages of bed evolution, when the bedforms are still very small in size, the streamlines are well aligned with the underlying topology of the sediment bed, however as the ripples continue to develop and grow in size, the flow eventually detaches at the crest and a recirculation region forms on the lee side of the ripples (Nelson *et al.* 1993). For the case of fully developed flows over immobile/fixed dunes, the size of the recirculation region is primarily a function of the crest height and extends (beyond

the crest) in the streamwise direction to about 4 to 6 times the crest height, measured as the elevation difference between the crest and the subsequent trough (Kadota & Nezu 1999, Yue *et al.* 2005, Coleman *et al.* 2006, Grigoriadis *et al.* 2009). Here we define the size of the recirculation region (l_R) to be the farthest downstream distance from the crest (not exceeding its downstream neighbour) where the minimum span-averaged streamwise component of velocity along the z -direction becomes negative.

Figure 7 shows the variation of the ratio l_R/\hat{h} with respect to span-averaged crest height, measured from crest to subsequent trough for case S2 beyond $t_b = 1000$ and for case S5 beyond $t_b = 2500$, when the bed becomes nearly span-invariant. We observe the size of the recirculation region to exhibit significant scatter, especially when the crest height is still relatively small $\hat{h} < 0.1$. The scatter is however reduced for larger values of \hat{h} when the bed advances and evolves at slower speeds and bedform-bedform interactions are reduced, allowing the flow to reach a more stationary state compared to earlier times with $\hat{h} < 0.1$. This relatively large scatter for $\hat{h} < 0.1$ may be a result of the evolving topology which continuously modifies the overlying flow as opposed to the fully developed flow over stationary dunes (Kadota & Nezu 1999, Yue *et al.* 2005, Coleman *et al.* 2006, Grigoriadis *et al.* 2009). We should also note that the size of the recirculation region in our simulations is larger than what is reported in the simulations and experiments over fixed dunes. This may be attributed to the different bedform geometry between the aforementioned published data and our simulations, specifically that the distance between the crest and the subsequent trough in our simulations of time evolving bedforms is larger by about 3 times than that corresponding to the fixed topology (Error! Reference source not found.f). Also, the Reynolds number of the present simulations is much lower (by about an order of magnitude) than those used in the experiments and simulations with fixed bedforms. Even though the bedform propagation speeds are more than two orders of magnitude smaller than the bulk flow velocity, we should note that the comparison with the fixed bed data may be affected by the mobility of the bed.

In addition to the aforementioned span-averaged data, we have also compute the recirculation length based on span and time-averaged data. That is, the already span-averaged velocity field is additionally time averaged (in the frame of reference of the bed) over a time span of 25 bulk units. We observe a difference of no more than a few percent between the span-averaged data and the span-and-time-averaged data. This implies that the large scatter for relatively small bedforms in Figure 7 is not a direct result of turbulent fluctuations. In fact, as we will discuss in sections 3.3 and 4, neighbouring structures could significantly impact bedform and flow dynamics and thus are likely the reason behind the relatively large scatter in Figure 7.

2.3 Temporal evolution of Fourier modes

Fourier analysis of the bed height variation is a natural and convenient way to quantify the wavy nature of the bed throughout the different stages of its development. It provides a quantitative method to track the apparent wavelength and amplitude of the sediment bed over time. It also provides a basis for comparing the rate of development of the bed as a function of grain diameter and shear velocity. In Figure 8, we show the time evolution of the amplitude of the first six modes for cases S1, S2, and S3. Here, we perform the streamwise Fourier transform of the bed height along each spanwise y location to obtain the amplitude and phase speed of each streamwise mode, and then average in the spanwise direction. In discrete form we obtain

$$F(n, y, t) = \frac{1}{N_x} \sum_{k=0}^{N_x-1} h(k\Delta x, y, t) \exp\left[-i\frac{2\pi kn}{N_x - 1}\right], \quad (4)$$

$$A(n, t) = \frac{1}{N_y} \sum_{l=0}^{N_y-1} |F(n, l\Delta y, t)| \quad \& \quad c(n, t) = \frac{1}{N_y} \sum_{l=0}^{N_y-1} \frac{\lambda_n}{2\pi} \frac{\partial}{\partial t} \{arg[F(n, l\Delta y, t)]\}. \quad (5)$$

Here F is the Fourier coefficient that encodes both the amplitude and phase of each of the $(N_x/2 + 1)$ modes (given by $n = 0, 1, 2, \dots, N_x/2$), $i = \sqrt{-1}$, and $\lambda_n = L_x/n$ corresponds to the wavelength of the n^{th} mode, where L_x is the size of the computational domain along the streamwise direction. This definition of amplitude and phase speed where y -average is taken after x -Fourier transform is appropriate as it accounts for spanwise variation in the ripple geometry. An average in the y -direction followed by a Fourier transform in the x -direction will be affected by spanwise incoherence of the ripples.

By tracking the spectral modes of the amplitude of bed height variation, we are able to provide a measure of the coarsening process and the spacing between bedforms. From Figure 8 we observe the rate of bedform evolution to be strongly dependent on the friction velocity of the flow. The time it takes for the amplitude of any of the modes of cases S1, S2, and S3 to grow to a value of approximately 0.02 is about 350 bulk time units, whereas for the lower shear velocity cases S4, S5, and S6, the time needed to attain the same value of amplitude is much larger at about 2000 bulk time units. Figure 8 also provides a quantitative measure for the coarsening of the bedforms. Consider for example case S2, where during the early stages of bedform development for $100 \lesssim t_b \lesssim 200$, the higher modes ($n = 4, 5, 6$) dominate, but with time the bedforms coarsen and progressively lower modes gain amplitude. The second mode M2 becomes the dominant mode after approximately $t_b = 2500$. Additionally, for a fixed value of the shear velocity, the time it takes for the bedforms to coarsen appears to depend on the grain size, where for smaller grains, the rate of wave coarsening is higher than that for larger grains. This is consistent with the fact that for the same shear velocity, the sediment volumetric flux is larger for smaller grains and hence the rate of bedform evolution is consequently faster (Coleman & Melville 1994).

Many studies suggest that the equilibrium wavelength of ripples scale with the grain size of the bed (e.g. Flemming 2000, Cladou & Andreotti 2006, Yalin 2013). It is difficult to currently assess whether such a dependence is captured in our simulations as the bedform is still slowly evolving even after integration over a long period. We can however observe some indication regarding the aforementioned scaling. Keeping in mind that cases with larger shear velocities and smaller sediment size will have a larger volumetric flux of sediment, and therefore will evolve toward the equilibrium state faster than cases with smaller shear velocities and larger sediment size, now let us focus on cases S1, S2, and S3 as these will evolve faster than S4, S5, and S6. For case S3, the dominant mode beyond $t_b = 1500$ is M3, corresponding to 3 waves within the computational domain. On the other hand, the dominant mode for case S2 beyond $t_b = 2500$ is M2, corresponding to 2 waves. Therefore, for these two cases, the scaling is consistent with the experimental observation of longer ripple wavelengths for larger sediment size. One may argue however that for case S1, the dominant mode at $t_b = 2500$ is M4 which does not follow the trend of S2 and S3, as one would expect the dominant mode to be at most M2. We must however note here that case S1 is the slowest of the three to develop and therefore we expect the higher modes (M3 and M4) to give way at later times in favor of M2 or even M1. We also need to keep in mind that because of the limited size of the periodic computational domain, we can only accommodate integer mode numbers. That is, while the largest possible wavelength is L_x , the next smaller possible wavelength is $L_x/2$, with no

in-between values permitted. The spectral counts of wavelengths do not necessarily capture the much smaller bedforms, but they are consistent with the manual counts of dominant bedforms. For example, for case S2, we clearly observe, beyond $t_b = 1500$, two dominant bedforms along with two much smaller bedforms.

The phase speed $c(n, t)$ in (5) provides a good measure of the speed of propagation of a specific mode, and indirectly the speed of the bed as a whole. Figure 9 shows the temporal evolution of the phase speed \tilde{c} for modes, M3 through M6, for case S2. Here \tilde{c} is the phase speed normalized by the bulk velocity, $\tilde{c} = c U_\tau^*/U_b^*$. At early times when the bed is still evolving, we observe $\tilde{c}(n, t)$ to be chaotic. In fact, when the amplitude of the modes is still very small, say $A(n, t) < 7 \times 10^{-3}$, the modes are very susceptible to fluctuations imposed by the turbulent bed shear stress. Once $A(n, t)$ grows large enough, we observe the fluctuations in \tilde{c} to decrease significantly. Consider mode M3 in Figure 8b whose amplitude only surpasses a value of 7×10^{-3} around $t_b = 500$, which corresponds approximately to the time when the fluctuations of \tilde{c} for mode M3 in Figure 10 are significantly reduced. We observe \tilde{c} to be nearly independent of the mode number and to be indicative of the velocity of the bed as a whole.

Once the bedforms are fully developed, the time evolution of the bed as a whole strongly resembles the evolution of a single spectral mode. In Figure 10, we plot the time evolution of the 4th mode M4 for the six cases, S1 through S6 beyond $t_b = 1000$, when the fluctuations for S4, S5, and S6 have sufficiently diminished. We observe the phase speed for the relatively high U_τ^* cases S1, S2, and S3 to be about 3 times larger than the low U_τ^* cases S4, S5, and S6. On the other hand, we observe \tilde{c} to be marginally affected by the grain size. The phase speed of the other modes is also qualitatively similar to that shown in Figure 10. Therefore, it appears that the phase speed of the different modes substantially varies over time as a result of the non-linear interaction between the different modes in terms of the bedform interactions.

2.4 Two-point correlation

A two-point correlation analysis of the bed provides a single effective value for bed wavelength and bed velocity as a function of time. These values may then be contrasted with those for the individual modes obtained from the Fourier analysis. In Figure 11, we present the dominant wavelength λ_{2p} as well as the bed velocity \tilde{c}_{2p} , which has been normalized by the flow bulk velocity. Here and in the remainder of the paper, the subscript 2p corresponds to a value obtained using the two-point correlation. The two-point correlation function $n_\lambda(\xi, t)$ of the bed elevation is defined as

$$n_\lambda(\xi, t) = \frac{\int_0^{L_y} \int_0^{L_x} h(x, y, t) h(x + \xi, y, t) dx dy}{\int_0^{L_y} \int_0^{L_x} h(x, y, t) h(x, y, t) dx dy}. \quad (6)$$

The dominant wavelength λ_{2p} is defined as the value of ξ at which the two-point correlation function attains its first peak. Here we discount the peak corresponding to $\xi = 0$. A representative plot of the two-point correlation function versus separation ξ is shown in Figure 11 as an inset at $t_b = 1220$ for case S2. The correlation function n_λ is normalized and thus has a maximum of unity. Because of periodicity in the streamwise direction, we only need to consider the separation ξ for half the domain length, i.e. $0 < \xi < L_x/2$ as n_λ is symmetric about $\xi = L_x/2 = 6$. The distance between $\xi = 0$ and the first and only minimum

(in this case) denoted by the vertical solid blue line at $\xi \approx 1.5$ corresponds to the dominant crest-to-subsequent-trough separation. On the other hand, the distance between $\xi = 0$ and the first and only maximum (for this specific case) denoted by the vertical dashed black line at $\xi \approx 3.5$, which is usually the highest peak of n_λ over the entire domain (excluding $\xi = 0$), represents the dominant wavelength λ_{2p} , i.e. the dominant crest-to-crest separation. For the time considered in the inset ($t_b = 1220$), the correlation function only exhibits a single minimum as well as a single maximum over the range $0 < \xi < L_x/2$. While this might be the case for relatively long time (i.e. $t_b \gtrsim 1200$), the correlation function n_λ displays multiple maxima and minima at earlier times, whose amplitudes usually decrease with increasing values of separation ξ . These multiple maxima and minima are indicative of the presence of multiple bedforms whose separation is inferred from the distance between these maxima and minima. We should note that if all the bedforms are perfectly periodic in the streamwise direction, then the amplitude of all the maxima (and minima) as well as their crest-to-crest (and crest-to-trough) separations would be identical.

At the very early stages of bed development, the bedform is very chaotic due to the dominant influence of the overlying turbulent flow, which results in large fluctuations in the value of λ_{2p} (Figure 11 for $t_b \lesssim 50$). However, once the chevron features begin to emerge, we are able to obtain meaningful values of λ_{2p} , where for all six cases considered, we see an increasing trend due to wave coarsening. Here as well, we observe the effect of the applied shear stress and the grain size on the development of the bed. During early times, for $t_b \lesssim 600$, we observe λ_{2p} for cases S1, S2, and S3 to increase faster by about a factor of 2 compared to cases S4, S5, and S6. We should note here that this faster rate does not explicitly depend on the bedload flux model we use. A smaller flux of sediment restricts the bed to slower evolution rate, hence the slower rate observed in Figure 11 for cases S4, S5, and S6. Additionally, at these early times, we observe the grain size to only marginally affect the value of λ_{2p} as well as its rate of increase. At later times, $t_b \gtrsim 1500$ for S1, S2, and S3 and $t_b \gtrsim 2200$ for S4, S5, and S6, we observe the effect of the grain size on λ_{2p} to become important. For case S1, because of the relatively larger grain size, λ_{2p} increases at a slower rate compared to cases S2 and S3. If the present simulations are to be representative of field observations and laboratory experiments, then we would expect λ_{2p} from case S1 to eventually be the larger of the three after the bed is given enough time to evolve. As mentioned earlier in §2.3, we observe an indication of this trend with cases S2 and S3 where λ_{2p} for case S2 is larger than that for case S3. As for the lower shear stress cases, S4, S5, and S6, they require much longer integration times to display the increasing wavelength scaling with grain size for equilibrium ripples. By $t_b \approx 2200$, we observe λ_{2p} for case S6 to peel off from the other two slowly evolving cases and approach λ_{2p} for case S3. In all the cases, the slow increase in λ_{2p} is clearly indicative of the slow coarsening trend exhibited by the ripples.

As the bedform coarsens the mean wavelength of the ripples and the ripple height accordingly increase. This process of growth is limited by the height of the ripple, either by altering the turbulence production process or through interaction with the free surface, or by reaching a critical velocity at the crest (Flemming 2000). Here we discuss near-equilibrium states, which remain stable for very long time, and consider properties of this near-equilibrium state, such as wavelength of the ripples and their dependence on grain size and flow depth.

For evaluating the effective phase speed of the bedform, we define the normalized space-time correlation as

$$n_c(\chi, \varsigma, t) = \frac{\int_0^{Ly} \int_0^{Lx} h(x, y, t) h(x + \chi, y, t + \varsigma) dx dy}{\int_0^{Ly} \int_0^{Lx} h(x, y, t) h(x, y, t) dx dy}. \quad (7)$$

For a fixed value of $\varsigma = 3 \times 10^{-2}$ we compute the space-time correlation and obtain the value of χ that maximizes n_c . The non-dimensional bed velocity is then obtained as $c_{2p} = \chi_{max}/\varsigma$. In [Figure 12](#), we show the time evolution of $\tilde{c}_{2p} = c_{2p} U_\tau^*/U_b^*$ for the six cases [S1](#) through [S6](#). This value of ς corresponds to a $\Delta t_b = 0.47$. Space-time correlation obtained for other values of ς remains qualitatively similar and the conclusions to be drawn are robust and insensitive to the above choice of ς .

A decreasing trend for the bed velocity over time as in the phase speed plot in [Figure 9](#) is observed. Here again, we note the marginal effect the grain size has on the celerity of the waves with very little differences observed among cases [S1](#), [S2](#), and [S3](#) and [S4](#), [S5](#), and [S6](#), respectively. On the contrary, we observe the bed shear stress, imposed by the overlying flow, to dictate the speed at which the bed evolves during all stages of bedform evolution. Additionally, at late times $t_b \gtrsim 2000$, the value of the bed velocity from cases [S1](#), [S2](#), and [S3](#) is approximately 3 times that from cases [S4](#), [S5](#), and [S6](#).

Finite amplitude ripples advance at a velocity c obtained from mass conservation on the lee side ([Coleman & Melville 1994](#), [Charru et al. 2016](#)) as

$$c = \frac{q}{\hat{h}}, \quad (8)$$

where q is the volumetric sediment flux per unit width at the crest and the ripple height, \hat{h} , is measured from the crest to the subsequent trough. In the inset of [Figure 12](#), we show the velocity \tilde{c}_{max} of the largest span-averaged ripple alongside \tilde{c}_{2p} for case [S2](#). Here, \tilde{c}_{max} is defined as

$$\tilde{c}_{max} = \frac{U_\tau^*}{U_b^*} \frac{\bar{q}_{max}}{\hat{h}_{max}}, \quad (9)$$

where \hat{h}_{max} is the maximum height of the span-averaged bed, measured from crest to subsequent trough and \bar{q}_{max} is the span-averaged sediment flux per unit width at the crest of the largest ripple. From the inset of [Figure 12](#), we find \tilde{c}_{max} to follow the same trend and to have a value that is close to but smaller than \tilde{c}_{2p} . Recall that \tilde{c}_{max} is based on the largest ripple and consequently is expected to be slower than the average velocity of the bed.

3. Ripple self-similarity

3.1 Shape self-similarity

[Yalin \(2013\)](#) argues that ripple development may be divided into two phases. During the first relatively short lived phase, ripples grow in both size and steepness. A growth in steepness indicates that the rate of growth of the height of the ripple is faster than the rate of growth of the ripple's length. On the other hand, during the second phase, ripples mainly grow in their size, i.e. in both height and length, maintaining a geometrically nearly similar shape. That is the ripple's height and length grow at comparable rates. In the following section, we find the bed evolution to match [Yalin's \(2013\)](#) hypothesis for the presence of

two phases during ripple growth. First recall that mature ripples are characterized by a gentle slope on the their stoss side and a steeper slope on their lee side equivalent to the angle of repose. Since the sediment bed is initially flat It follows that the ripple must initially steepen and as the ripple grows the slope on the lee side plateaus toward the angle of repose. Additionally, once the slope on the lee side approaches the angle of repose, we observe the ripples to grow in size, while maintaining a nearly self-similar profile.

Once the bed becomes nearly span-invariant, a vertical slice of the bed may be used to quantify the shape of the bed in the entire domain. [Figure 13](#) shows a ripple from the cross section of the bed in the $y = L_y/2$ centre plane for all S^* cases in [Table 2](#). Two times are considered, namely $t_b = 1500$ and $t_b = 2500$. In each case, the ripple is translated along the streamwise direction by a distance that corresponds to the location of the crest (x_{crest}). In order to align the ripple crests in the plot, the ripple height for each case is also scaled both in the streamwise and vertical directions by the respective crest height (h_{crest}). Except for cases [S4](#) and [S5](#) at $t_b = 1500$, the ripples demonstrate a nearly self-similar triangular-like profile with a gentle slope on the stoss side and a steeper lee side dictated by the angle of repose ($\alpha_R = 30^\circ$). The thick solid orange line overlaying the stoss side of the ripples provides an estimate for the slope which corresponds approximately to a 6° angle. Alternatively, the thick orange line on the lee side has a slope which corresponds to the imposed angle of repose. As can be clearly seen in [Figure 13](#), cases [S4](#) and [S5](#) at the early time of $t_b = 1500$ deviate from the self-similar profile. The slopes on both sides of the crest for these cases are smaller than those observed for the self-similar profile. Recall that these 2 cases correspond to the lower bed shear stress value and relatively larger grain diameter (see [Table 2](#)). Therefore, on average, the volumetric flux of sediment is the lowest for these 2 cases, and consequently the ripples are slow to develop. Thus these two profiles haven't reached their self-similar state by $t_b = 1500$.

On the other hand, for the same 2 cases, [S4](#) and [S5](#) at the later time of $t_b = 2500$, the ripples demonstrate the aforementioned triangular self-similar shape. By this time, the vertical drop from the crest to the subsequent trough of the tallest ripple is 0.08 and 0.09 for [S4](#) and [S5](#), respectively. Whereas at $t_b = 1500$, the vertical drops were approximately two times smaller at 0.05 and 0.04 for [S4](#) and [S5](#), respectively. In fact, all the ripples in [Figure 13](#) that exhibit the self-similar profile, the vertical drop from the crest to the subsequent trough was above 0.08. This suggests that there is a minimum vertical drop above which the cross-sectional shape of the ripple approaches the self-similar profile. Additionally, the self-similar profile displayed in [Figure 13](#) may only be reached once the slope on the lee side corresponds to the angle of repose. Furthermore, by inspecting over 250 ripples at various stages of evolution for the six S^* cases, we find this minimum or threshold vertical drop to be around 0.07, which is equivalent to about 4, 7, and 20 grains for [S1](#), [S2](#), and [S3](#), respectively.

We have considered the cross-sectional shape of the different ripples that are present in a bed at a specific instant during bed development (for example the 5 ripples seen in Figure3k in [paper I](#)) and the cross-sectional shape of the same ripple as it evolves over time (for example the ripples that are tracked in Figure3 ([paper I](#)) from frame k to frame l). We have also considered the variation in the shape of the ripple from one bed to the other where the flow conditions are kept unchanged, but sediment properties, such as sediment size, are modified ([S1](#) vs [S2](#) vs [S3](#)). Alternatively, for different flow conditions but with identical sediment properties ([S1](#) vs [S4](#)). In all these cases, once the height of the ripple grows large enough such that the lee side corresponds to the sediment angle of repose, the cross-sectional shape of the ripple is observed to conform to the triangular self-similar shape. This self-similar shape appears to be

independent of grain size and flow conditions (Simons 1960). The stoss side of the self-similar profile has an inclination of about 6° , which is consistent with previous studies using direct numerical simulations (Kidanemariam & Uhlmann 2017) and experiments in the field (Fourriere et al. 2010), whereas the slope at the lee side is dictated by the angle of repose. In fact a necessary condition for self-similarity is the development of an avalanche slip-face (corresponding to the angle of repose) on the bedform's lee side.

In fact, we observe the cross-sectional shape of isolated mature ripples to exhibit a self-similar profile. However, at later times, as the crest height of such ripples decay in amplitude due to bedform-bedform interactions for example, we find their cross-sectional profile to progressively deviate from self-similarity. This supports the observation that ripples maintain a self-similar shape provided their height is larger than the aforementioned threshold height of 0.07 non-dimensional units. In other words, ripples as they grow in size take a self-similar shape when their size exceeds a threshold, and ripples as they decay in size, lose their self-similar shape when their size falls below a threshold value. If flow conditions and sediment availability are maintained, then bedforms will only decay when acted upon by upstream neighbours. That is a mature ripple that is sufficiently far from an upstream neighbour will remain self-similar until it is “preyed” upon by an upstream neighbour or experiences a change in flow conditions or sediment availability. We will elaborate on the conditions that cause developing ripples to deviate from self-similarity in the next section.

3.2 *Bed shear stress self-similarity*

Owing to the fact that the Exner equation is used to evolve the sediment bed, it follows that for the ripple cross-section to attain and maintain a self-similar shape, the sediment flux and consequently the bed shear stress must also be self-similar. With that in mind, we have considered in Figure 14a the cross-sectional shape (denoted by symbols) of three self-similar ripples from cases S1, S2, and S3 along with the associated bed shear stress profiles (denoted by lines) at $t_b = 744$. Unlike the cross-sectional shape of ripples which evolves on a much longer time scale compared to the overlying flow field, the bed shear stress is inherently turbulent with substantial local and instantaneous fluctuations mirroring the passing of near-bed intense turbulent eddies. Therefore, instead of showing an instantaneous cross-section of a ripple with its turbulent bed shear stress profile, we make use of the nearly span-invariant bedforms to average in the spanwise direction. Additionally, because of the separate timescales over which the bed and the flow evolve, we average the shear stress within a sufficiently small time window of 7 bulk time units, during which the ripple translates by less than one grid cell. The time over which the averaging is performed needs to be large enough to filter out the local and instantaneous fluctuations, but small enough such that the flow sees a stationary ripple. Time averaging, which is denoted in the figure by the angular brackets, is only needed for the shear stress profiles, however to remain consistent, we also average the bed height variation \bar{h} over the same time period. Here again, the bed height variation is normalized by the span and time averaged crest height, $\langle \bar{h}_{crest} \rangle$. Similarly, we scale the span and time averaged shear stress $\langle \bar{\tau} \rangle(x, t)$ by the instantaneous bed-averaged shear stress $\bar{\tau}(t)$. Similar to Figure 13, we observe the averaged ripple cross-sections to exhibit the same self-similar triangular profile. Additionally, the profiles of the shear stress are also found to be nearly self-similar with an analogous triangular shape displaying a gentle rise on the stoss side of the ripple, followed by a steep drop in the region approximately one ripple height around the crest of the ripple, which is further followed by a slow drop in the shear stress for the remainder of the lee side. The time and location of the ripples in the figure

are chosen such that they are sufficiently far from upstream and downstream neighbours so that they may be considered locally isolated in the sense that the overlying flow field is weakly or negligibly influenced by the presence of neighbouring structures. Neighbouring structures, as we will shortly see, can significantly alter the overlying flow field and consequently the bed shear stress profiles. We should also note the presence of the positive phase shift between the shear stress and cross-sectional shape of the ripple at the crest. The maximum shear stress does not occur at the crest but slightly upstream towards the end of the stoss side. This phase shift is primarily responsible for the growth of the ripple. While sediment inertia, in the context of coarse sediments, has been used as a possible explanation for the presence of such a phase shift in laboratory experiments (Parker 1975), here we observe the phase shift to come out naturally from the hydrodynamic nature of the flow.

To further illustrate how bedform-bedform interactions cause a self-similar ripple to deviate from self-similarity, we show in [Figure 14b](#) the same cross-sectional shape of the self-similar ripple from [S2](#) at three time instances, namely $t_b = 744, 2350$, and 2501 . The first time instance ($t_b = 744$) is the same as that shown in frame a and corresponds to the self-similar profile. The subsequent instances are chosen at a time when a smaller upstream neighbour (blue symbols) approaches the stoss side of the ripple in question. As can be seen from the figure, the upstream neighbour is smaller and thus able to catch up to the self-similar ripple. In addition to the obvious deformation this smaller upstream ripple causes to the cross-sectional shape of the self-similar ripple, it also significantly modifies the shear stress over the entire stoss side of the ripple. For example, the shear stress at $(x - \langle \bar{x}_{crest} \rangle)/\langle \bar{h}_{crest} \rangle = -15$ is reduced by approximately 3 to 5 times by $t_b = 2350$ and 2501 , respectively compared to the self-similar profile at $t_b = 744$. While the deviation from self-similarity in terms of the cross-sectional shape needs time to develop, the shear stress profiles are rapidly modified on the turbulent flow timescale. These new modified shear stress profiles now act to modify the bedload fluxes on the stoss side eventually leading to a departure of the ripple from its self-similar shape. These examples highlight the approach to self-similarity of a ripple and departure from self-similarity when acted upon by an upstream neighbour.

3.3 Characterization of the self-similar state

One of the characteristics of ripples is their asymmetrical triangular shape in which the slope on the stoss side corresponds to a few degrees, while the slope on the lee side is much steeper and is usually dictated and corresponds to the angle of repose of the sediment grains. Here we provide a very simple and crude analysis to estimate the slope of the stoss side from the self-similar shear stress profiles. In [Figure 15](#), we show a schematic of a two-dimensional self-similar ripple undergoing pure translational motion. The solid black line corresponds to the profile of the ripple at time t , while the red dashed line corresponds to the profile at a later time $t + \Delta t$ where the ripple has translated along the streamwise direction by a distance $c \Delta t$. To simplify matters, we consider the ripple speed c to be a temporally and spatially independent constant, additionally the ripple does not grow or decay, but rather keeps the exact same cross-sectional shape and simply translates downstream. Since we are interested in extracting the bed slope on the stoss side, we compute the height variation as

$$\frac{\Delta h}{\Delta t} = c \tan \theta , \quad (10)$$

where θ is the inclination on the stoss side of the ripple. It follows from the Exner equation (as $\Delta t \rightarrow 0$) that if we neglect the diffusion term, the inclination of the stoss side may be expressed as

$$\theta = -\tan^{-1} \left(\frac{1}{c\varphi} \frac{dq}{dx} \right), \quad (11)$$

where φ corresponds to the volume fraction of the sediment bed and q is the volumetric flux of sediment due to bedload. By considering the cross-section of a self-similar ripple from S3 at $t_b = 2009$ in Figure 16 along with the span and time averaged (over the same small period of 7 bulk time units as in Figure 14) x -component of the volumetric flux of sediment q_x , we extract the spatial variation ($d\langle q_x \rangle / dx$) on a portion of the stoss side bounded by the vertical thin dashed lines such that it is sufficiently far from the crest and the base of the stoss side. By substituting for the values on the right hand side in (11), we find $\theta \approx 5^\circ$, which is consistent with the actual computed inclination of the stoss side of a self-similar ripple of $\theta \approx 6^\circ$ in Figure 13 as well as previously published data (Kidanemariam & Uhlmann 2017). Equation (11) also indicates that for a ripple to retain its self-similarity as it evolves, the ripple speed and the spatial variation of the bedload flux must vary proportionally with one another.

Once the ripples attain a self-similar profile, their height and wavelengths become strongly interdependent in such a way that as the bedforms coarsen, their height, measured from crest to subsequent trough, must also proportionally increase. For each ripple that has grown to its self-similar shape we define its wavelength $\hat{\lambda}$ as the streamwise distance between its upstream and downstream troughs. Correspondingly the ripple height \hat{h} is defined as vertical distance between the crest to the downstream trough. In Figure 17, we plot $\hat{\lambda}$ versus \hat{h} only for self-similar ripples from cases S1 through S6. We observe the wavelength to height ratio of the ripples in the self-similar phase to be approximately 25, consistent with previously reported data from direct numerical simulations of Kidanemariam & Uhlmann (2017) as well as laboratory experiments and field studies (Flemming 2000). The dashed line in Figure 17 corresponds to an aspect ratio of 20, which has been reported by Andreotti & Claudin (2013). They argue that when the ripple aspect ratio approximately reaches this value, the ripple amplitude saturates and the slope on the lee side of the ripple corresponds to the angle of repose.

The spectral and two-point correlation analyses showed that the speed of the bedform decreased over time, while the mean wavelength and height of the ripples increased. Here we will directly quantify the correlation between ripple height and ripple velocity and compare the simulation results against previous laboratory experiments. Coleman & Melville (1994) conducted a series of laboratory experiments with sand particles with mean grain size of $200\mu m$ and $820\mu m$. They observed the speed of the rippled bedform to be inversely proportional to the ripple height and proposed the following empirical fit:

$$\hat{c}(\hat{h}^*/d_p^* - 3.5)^{1.3} = 40, \quad (12)$$

where they defined the non-dimensional ripple speed \hat{c} as

$$\hat{c} = \frac{c^*}{(u_t^* - u_{t,cr}^*)(\Theta - \Theta_{cr})}, \quad (13)$$

where $u_{t,cr}^*$ represents the critical shear velocity. Venditti (2003) conducted similar experiments in a flume with sand particles of mean grain size $500\mu m$. In Figure 18, we show a plot of \hat{c} vs \hat{h}/d_p from the present simulations S1 through S6 as well as from the laboratory experiments of Coleman & Melville (1994) and

Venditti (2003). The data points for our simulations were only obtained for ripples in the self-similar phase. To obtain the ripple speed \hat{c} from the simulations, we span average the bed, after it has become nearly span invariant, and track the largest ripples that exhibit a self-similar profile. For these ripples, we compute the temporal evolution of the streamwise speed of the crest, as well as the vertical drop between the crest and the subsequent trough. We observe good agreement between the simulation data and the empirical fit of Coleman & Melville (1994) for values of $\hat{h}/d_p > 20$, and reasonable agreement for smaller values of \hat{h}/d_p , where the present data lies below the empirical fit. We note however that the values that do not fall exactly on the proposed fit are still within the experimental data scatter reported in Coleman & Melville (1994) and Venditti (2003). Additionally, we find our data to correspond more closely to the following empirical fit

$$\hat{c} \frac{\hat{h}}{d_p} \ln \left(\frac{\hat{h}}{d_p} \right) = 45. \quad (14)$$

From Figures 17 and 18, it can be observed that the streamwise size (or wavelength) of a ripple and its speed are primarily influenced by the ripple height. However, these plots also suggest that additional factors besides the crest height could also affect the size and the speed of the ripples. The large scatter in Figure 18 and also the scatter seen in the wavelength versus wave height plot indicate imperfect correlation between these quantities. Indeed, the scatter in Coleman & Melville (1994) data can at times exceed a factor of four, which seems too large to simply attribute to experimental uncertainty. Similarly, the scatter in our simulation results is also not due to numerical noise. We observe the presence and proximity of neighbouring bedforms downstream and upstream to play a key role in dictating the wavelength and speed of every bedform. It is clear that for a ripple, the approach of an upstream or downstream ripple close to it will result in a decrease of its wavelength, defined as the distance between the upstream and downstream troughs. It was demonstrated in Figure 14 that the effect of an upstream neighbour can be significant in terms of local bedload transport of sediment on the stoss side. It appears that the proximity of neighbouring structures through such interactions also leads to substantial variation in the ripple speed. In fact, interactions between neighbouring ripples is the main cause of ripple growth and decay, and in general the ripple dynamics. These aspects will be further addressed in the following section.

4. Bedform coarsening

Bedform coalescence or wave coarsening occurs when two separate bedforms interact or come together to produce a single discrete structure (Raudkivi & Witte 1990). Because the speed of bedforms is inversely proportional to their height, bedform coarsening is generally initiated by an upstream smaller structure approaching a larger downstream structure. Consequently, for coarsening to occur, one of the two interacting structures must grow while the other must diminish and gradually disappear (Coleman & Melville 1994). The first possibility is for the upstream bedform to ride up the stoss side and merge with the larger downstream structure, a mechanism that is identical to the merging sequence involving defects described in paper I. However unlike defects, here merging occurs across the entire span of the interacting bedforms, i.e., for the entire nearly span-invariant ripple. The second possibility is for the upstream structure to grow by starving the downstream neighbour. This mechanism is yet again identical to bedform repulsion (described in paper I), but occurs across the entire span of the interacting bedforms. The first of the two possibilities, merging, usually occurs when the upstream neighbour is too small to starve the larger downstream structure. This is usually a result of a limited sediment supply caused by a

non-eroding flow on the base of the stoss side of the upstream neighbour. The second possibility, which consists of the upstream structure starving its downstream neighbour, occurred more often in the simulations and was also found to be a predominant (over the first) coarsening feature in the experiments of Coleman & Melville (1994). Additionally, when this starving process occurs, the starving/diminishing bedform could be either absorbed by the upstream growing neighbour, or alternatively, could temporarily escape and merge with a larger downstream structure. But this second scenario is the same as first possibility where a weak ripple merges with its downstream neighbour, but in this case this merging process is driven by the upstream neighbour of the weak ripple. In other words, a third ripple which is not involved in the merging process is driving the interaction, which can be considered as remote interaction.

In the remainder of this section , we consider the ripples from case S2 as we track the coarsening process that progressively leads to fewer and larger bedforms. Figure 19 shows a spanwise-averaged side view of the bed with iso-contours of the streamwise component of velocity \bar{u}_x at $t_b = 515$. We identify five ripples, in which the crests and corresponding troughs are marked sequentially by C_n and T_n (with n going from 1 to 5), respectively. The height of the first three ripples are large enough to induce substantial flow separation on their lee side. At this time, the bedforms span the entire width of the domain and have become nearly spanwise-invariant/two-dimensional, except for ripple 5, which from a top view of the bed appears to be rather sinuous. In fact, the degree of two-dimensionality may be inferred from the overall shape of the ripple as well as the slopes on the stoss and lee sides. For example, the slope on the lee side of ripple 5 is almost equivalent to that on its stoss side, and the ripple's cross-sectional shape resembles more a symmetric isosceles triangle than the characteristic asymmetric triangular shape. This indicates that the crest line C_5 is not straight but rather sinuous so that the spanwise-averaged slope is nearly identical downstream and upstream of the crest.

The coarsening sequence of case S2 is investigated by tracking the subsequent interactions among the five bedforms beyond the time shown in Figure 19. In Figure 20, we show a time series of the spanwise-averaged bed revealing a remote interaction between C_4 and C_5 . The interaction is illustrated through four time instances. From the cross-sectional view in Figure 20a, we observe C_4 to be smaller than C_5 and thus approaches the latter. As discussed earlier, when the separation between the bedforms decreases beyond a certain threshold, there are two possible outcomes for which either C_4 or C_5 survives after the interaction. In this particular situation, C_4 is sufficiently far away from C_5 such that it is able to grow and starve its downstream neighbour C_5 as shown in Figure 20b. Recall that the domain is periodic in the streamwise direction such that ripple C_4 is still upstream of C_5 in Figure 20b. The continuously diminishing crest C_5 is pushed away towards C_1 , and as can be seen by the elongated stoss side of ripple 1 in frame d (relative to frame c), C_5 merges with its downstream neighbour C_1 . In fact, by looking at videos of the simulations for other cases, we find that the diminishing ripple (C_5 in the present case) merges with its downstream neighbour (C_1 in the present case) when the latter is sufficiently close. On the other hand, if the downstream neighbour (C_1 in the present case) is not close enough, the diminishing ripple is unable to escape in time and becomes part of the trough of the upstream neighbour (C_4 in the present case). Such a scenario is later observed in the coalescing remote interaction between C_4 and C_1 (not shown here), in which C_4 starves and gobbles up the latter.

4.1 Ripple statistics

We can analyse ripple statistics by identifying each ripple by its crest and its downstream trough, where by definition, each crest is separated from its upstream and downstream neighbours by a trough. Due to its self-similar shape, each crest will be characterized by its span-averaged height \bar{h}_c and its span-averaged streamwise location \bar{x}_c . Correspondingly, each trough will be denoted by its depth (negative height $-\bar{h}_t$ below the mean bed elevation) and its streamwise location \bar{x}_t (see [Figure 20a](#)). Time histories of \bar{x}_c , \bar{h}_c , \bar{x}_t , and \bar{h}_t for all the crests and troughs of case S2 are shown in [Figure 21](#) frames a, c, d, and f, respectively. Also shown in the figure are $d\bar{x}_c/dt$ and $d\bar{x}_t/dt$, which correspond to the span-averaged velocity of the crest and the trough, respectively. Whenever one of the lines in each frame is discontinued, a coarsening/coalescing interaction takes place in which a peak disappears, with the corresponding disappearance of either its upstream or downstream trough, depending on the nature of the interaction. The first crest and trough to disappear are those corresponding to C₅ and T₅, respectively. The other interacting bedform in this coarsening process is ripple 4. Let us examine the speeds and elevation of those two bedforms during the interaction. From [Figure 21b](#), we observe the speed of C₄ to decay while that of C₅ to rise, where the rates of decay and rise are roughly similar. Additionally, we observe the crest elevation of C₄ in [Figure 21c](#) to rise, while that of the diminishing ripple C₅ decreases, again at roughly the same rate. Moreover, we observe the trough T₄ to rise, toward the initial mean elevation, in accordance with ripple 4 acting to starve and absorb its downstream neighbour C₅. Similarly, in a subsequent interaction around $t_b = 2700$ between C₁ and C₄, we observe the same dynamics with regards to ripple speed and elevation of the interacting bedforms. The speed of the upstream neighbour C₄ momentarily decreases, while its crest elevation increases and its trough depth approaches the initial mean bed height. On the other hand, the speed of the diminishing downstream neighbour C₁ increases while its crest height drops. In both these instances, a finite ripple vanishes and consequently the number of bedforms in the domain is reduced.

To assess the effect of the coarsening interaction on the dynamics of ripples, specifically on the relation between height and speed, we evaluated the speed of the ripples involved in a coarsening interaction based on the empirical relation in [\(14\)](#). We found a relatively large discrepancy between the computed values from [\(14\)](#) and the observed values in the simulations. For example, at $t_b = 787$, which corresponds to the side view of [Figure 20b](#) where ripples 4 and 5 are in the process of coalescing into a single ripple, we find the crest speeds of C₄ and C₅ as predicted by [\(14\)](#) to be about three and five times larger than the actual speeds in [Figure 21b](#), respectively. On the other hand, for a ripple not currently involved in any coalescing interaction such as C₂, we find the speed of the crest predicted by [\(14\)](#) to be within 10% of the actual speed in [Figure 21b](#). This large discrepancy between the predicted and actual velocities for interacting bedforms is likely to contribute to the relatively large scatter observed in [Figure 18](#). Therefore, while the crest height remains the principal factor that dictates the ripple speed, neighbouring structures may temporarily and significantly influence the rate of propagation of ripples as they come into close proximity with the bedform in question. In addition to altering the ripple speeds, neighbouring structures also strongly influence the growth/decay rates of adjacent bedforms.

Finally, we note that the time needed to complete the coalescing interaction is much longer (up to 10 times) than that needed to complete the defect-related interactions during the early times of bed evolution (discussed in [paper I](#)) ([Perillo et al. 2014](#)). This is consistent with the fact that during the later

stages of bed evolution, the bedforms are larger in size (i.e. move relatively slow) and are more spaced out (i.e. must cover larger distances to interact with a downstream or upstream neighbour). This is contrary to the bed at early times, which is characterized by relatively small, closely spaced structures. It is important to note that in field observations ([Ewing & Kocurek 2010](#)), certain interactions involving very large scale bedforms can take up to decades to complete, while other interactions involving small ripples can occur in seconds or minutes.

5. Discussion

There is a clear distinct behaviour between the two sets of simulations in [Table 2](#), namely [S1 - S3](#), and [S4 - S6](#). A natural question that arises is whether this is a physical result or some consequence of the modelling employed in the present study, specifically the modified Meyer-Peter and Müller ([1948](#)) bedload relation of Wong & Parker ([2006](#)). The only difference between the two sets of simulations is that in the latter ([S4 - S6](#)) the friction velocity has been decreased, while the flow depth has been accordingly increased so as to maintain the same shear Reynolds number Re_τ . The two series however exhibit different bedform propagation velocities, different wavelengths, etc.

It is observed that the nondimensional bedform propagation velocity (scaled with the shear velocity) decreases with increasing shear velocity between set S1-S3 simulations to set S4-S6 simulations. Let us consider a limiting case for which the flow depth is very large and the bed shear velocity is very small so as to maintain a constant Re_τ . The critical shear velocity necessary for incipient motion is now much larger than the bed shear velocity, and consequently, there should be no sediment motion, or in other words, the bedform propagation velocity should be zero. Starting from this limiting case, let us gradually increase the bed shear velocity (while simultaneously decreasing the flow depth). There will come a point where the bed shear velocity would exceed the critical shear velocity necessary for incipient motion, and the sediments would be set in motion.

The non-dimensional parameter that is responsible for this distinct behaviour is the Shields number Θ or more specifically, the ratio of the Shields number to the critical Shields number necessary for incipient motion (Θ/Θ_{cr}). This dependence on Θ/Θ_{cr} is captured in the MPM (and consequently in the Wong & Parker modified MPM) formulation and is responsible for the distinct behaviour between the two sets of data. This can also be explained in terms of the three length scales: the channel height, wall unit (v/u_*) and the particle diameter. In both sets, the ratio of channel height to wall unit remains the same, since Re_τ is a constant. Thus, as the channel got taller the near wall eddies also correspondingly became bigger. However, if the particle size is kept the same, with decreasing U_τ^* the ability of the turbulent flow to move the particles changes.

6. Conclusions

Coupled bed-flow direct numerical simulations presented in [Part I](#) describe the early stages of pattern formation by ripples in an open channel flow analysed using a highly resolved flow field. In the present paper (Part II), we compare the simulations to published experimental data and quantitatively analyse the bed using spectral analysis and two-point correlations. The effect of the mobile rippled bed on the flow structure as well as turbulence was investigated locally (at specific streamwise locations) as well as over the entire computational domain. We showed that developing ripples attain a self-similar profile in both the shape and the corresponding bed shear stress profile. We further demonstrated the importance of neighbouring structures, especially upstream neighbours, on bedform dynamics in terms of the growth,

decay, and speed of ripples. Finally, we examined the defect-free interactions in the later stages of bed evolution, which primarily lead to wave coarsening.

Analysis of turbulence statistics indicates no qualitative difference in velocity fluctuations or the Reynolds stress profiles from a rippled and completely flat bed. However, velocity fluctuations increased near the bed at the expense of the mean flow as the ripples grew. Applying a logarithmic-law velocity profile for the span-averaged streamwise component of velocity in the far field yields an intercept which follows a trend similar to open channel flows with small scale roughness. Accurate calculation of the velocity fluctuations and Reynolds stresses requires the application of a coordinate frame, that it is normal to the bed in the near bed region and turns to the vertical direction sufficiently far away.

A quantitative analysis of the emerging bedforms revealed a -3.75 power decay for large wave numbers in the spectra for developing ripples. Similar values were obtained in previous direct numerical simulations of Kidanemariam & Uhlmann (2017). The decay is however faster than the -3 decay reported in the earlier experiments of Hino (1968), Jain & Kennedy (1974), and Nikora *et al.* (1997). The shear Reynolds number in the present study and from the numerical simulations of Kidanemariam & Uhlmann (2017) were more than an order of magnitude smaller than those calculated from the aforementioned experiments suggesting a possible Reynolds number dependence for bedform spectra.

Analyses from Fourier decomposition and two-point correlations of ripple properties such as crest height, wavelengths, and celerity indicated that the ripples increase in height and coarsen with time, with the speed of the ripple being inversely proportional to its crest height. Additionally, as the ripple height, measured as the elevation difference between the crest and the subsequent trough, increases beyond a threshold value, we observe the ripples to approach a nearly self-similar triangular-like shape characterized by a gentle stoss side of about 6° and a steeper lee side dictated by the angle of repose. Within this self-similar phase, we find the relationship between the ripple speed and height to agree with the empirical relation proposed by Coleman & Melville (1996). The self-similarity in the ripple shape is accompanied by an analogous self-similar triangular-like bed shear stress profile. There is however a positive phase shift between the streamwise location of the crest and the location of the maximum of the shear stress profile, for which the latter occurs slightly upstream of the crest. Through a simple and very crude analysis of the self-similar shear stress profile on the stoss side of the ripple, we are able to recover the computed gentle slope on the stoss side suggesting that the shape and bed shear stress profiles are strongly coupled.

The experimental data of Coleman & Melville (1996) exhibit considerable scatter around their aforementioned empirical fit. This scatter appears too large to be simply attributed to experimental uncertainty, but is likely a result of bedform-bedform interactions. Based on the present simulations, we find the relationship between the speed and the size of isolated mature ripples to follow the empirical fit of Coleman & Melville (1996), however when neighbouring ripples get within close proximity of the ripple in question (for which a relationship between the ripple speed and size is sought), we find the actual speed to significantly deviate from the speed predicted by the proposed fit by up to five times.

Of the six simulations considered, those with higher bed shear velocities (cases S1-S3) evolved faster than those with larger flow depths but smaller bed shear velocities (cases S4-S6) owing to their larger volumetric flux of sediment. While bed shear velocity is the principal factor dictating the velocity of the bed for the entire duration of the simulations, we find that grain size has only a marginal effect.

Cases with higher bed shear velocities coarsen at a faster rate compared to cases with lower bed shear velocities. On the other hand, at later times toward the end of the simulations, there is an indication that ripple wavelength scales with the grain diameter, with smaller sediment exhibiting smaller wavelengths. The current work could be improved by considering the following two factors. Firstly, ripples did not reach an equilibrium state by the end of the simulations even after long time integration of 3000 bulk time units because the purpose of these runs was to examine ripple initiation and early time evolution ([Paper I](#)) as well as ripple dynamics in the developing stage before reaching equilibrium. Secondly, these simulations lack essential physics, such as the saltation mechanism, for capping crest growth, and may therefore be inappropriate for studying the equilibrium stage of ripple evolution, but are suitable for investigating developing ripples during the period in which bedload constitutes the dominant mode of sediment transport.

Acknowledgement

We are grateful to ExxonMobil Upstream Research Company for providing support through grant number EM09296. Numerical data presented herein will be available in the Sediment Experimentalists Network (SEN) Knowledge Base (<http://www.sedexp.net>).

REFERENCES

- Andreotti, B., & Claudin, P. (2013). Aeolian and subaqueous bedforms in shear flows. *Phil. Trans. R. Soc. A*, 371(2004), 20120364.
- Andrle, R. (1996). THE WEST COAST OF BRITAIN: STATISTICAL SELF-SIMILARITY VS. CHARACTERISTIC SCALES IN THE LANDSCAPE. *Earth Surface Processes and Landforms*, 21(10), 955-962.
- De Angelis, V., Lombardi, P., & Banerjee, S. (1997). Direct numerical simulation of turbulent flow over a wavy wall. *Physics of Fluids*, 9(8), 2429-2442.
- Ashley, G. M. (1990). Classification of large-scale subaqueous bedforms: a new look at an old problem-SEPM bedforms and bedding structures. *Journal of Sedimentary Research*, 60(1).
- Balachandar, R., Polatel, C., Hyun, B. S., Yu, K., Lin, C. L., Yue, W., & Patel, V. C. (2003). LDV, PIV and LES investigation of flow over a fixed dune. In *Sedimentation and Sediment Transport* (pp. 171-178). Springer Netherlands.
- Barabási, A. L., & Stanley, H. E. (1995). *Fractal concepts in surface growth*. Cambridge university press.
- Bennett, S. J., & Best, J. L. (1995). Mean flow and turbulence structure over fixed, two-dimensional dunes: Implications for sediment transport and bedform stability. *Sedimentology*, 42(3), 491-513.
- Best, J. (1992). On the entrainment of sediment and initiation of bed defects: insights from recent developments within turbulent boundary layer research. *Sedimentology*, 39(5), 797-811.
- Best, J., & Kostaschuk, R. (2002). An experimental study of turbulent flow over a low-angle dune. *Journal of Geophysical Research: Oceans*, 107(C9).
- Chan-Braun, C., García-Villalba, M., & Uhlmann, M. (2011). Force and torque acting on particles in a transitionally rough open-channel flow. *Journal of Fluid Mechanics*, 684, 441-474.

- Charru, F., Andreotti, B., & Claudin, P. (2013). Sand ripples and dunes. *Annual Review of Fluid Mechanics*, 45, 469-493.
- Charru, F., Bouteloup, J., Bonometti, T., & Lacaze, L. (2016). Sediment transport and bedforms: a numerical study of two-phase viscous shear flow. *Meccanica*, 51(12), 3055-3065.
- Charru, F., & Mouilleron-Arnould, H. (2002). Instability of a bed of particles sheared by a viscous flow. *Journal of Fluid Mechanics*, 452, 303-323.
- Coco, G., & Murray, A. B. (2007). Patterns in the sand: From forcing templates to self-organization. *Geomorphology*, 91(3), 271-290.
- Claudin, P., & Andreotti, B. (2006). A scaling law for aeolian dunes on Mars, Venus, Earth, and for subaqueous ripples. *Earth and Planetary Science Letters*, 252(1), 30-44.
- Coleman, S. E., & Melville, B. W. (1994). Bed-form development. *Journal of hydraulic engineering*, 120(5), 544-560.
- Coleman, S. E., & Melville, B. W. (1996). Initiation of bed forms on a flat sand bed. *Journal of Hydraulic Engineering*, 122(6), 301-310.
- Coleman, S. E., & Nikora, V. I. (2011). Fluvial dunes: initiation, characterization, flow structure. *Earth Surface processes and landforms*, 36(1), 39-57.
- Coleman, S. E., Nikora, V. I., McLean, S. R., Clunie, T. M., Schlicke, T., & Melville, B. W. (2006). Equilibrium hydrodynamics concept for developing dunes. *Physics of Fluids*, 18(10), 105104.
- Einstein, H.A., Barbarossa, N. (1952) River channel roughness. Trans. ASCE **117**, 1121–1146.
- Engelund, F. (1977) Hydraulic resistance for flow over dunes. Inst. Hydrodyn. and Hydraulic Engrg. Tech. Univ. Denmark, Proc. Rep. **44**, 19–20.
- Ewing, R. C., & Kocurek, G. A. (2010). Aeolian dune interactions and dune-field pattern formation: White Sands Dune Field, New Mexico. *Sedimentology*, 57(5), 1199-1219.
- Fedele, J. J., & García, M. H. (2001). Alluvial roughness in streams with dunes: A boundary-layer approach. In *River, coastal and estuarine morphodynamics* (pp. 37-60). Springer Berlin Heidelberg.
- Flemming, B. W. (2000, March). The role of grain size, water depth and flow velocity as scaling factors controlling the size of subaqueous dunes. In *Marine Sandwave Dynamics, International Workshop* (pp. 23-24).
- Fourriere, A., Claudin, P., & Andreotti, B. (2010). Bedforms in a turbulent stream: formation of ripples by primary linear instability and of dunes by nonlinear pattern coarsening. *Journal of Fluid Mechanics*, 649, 287-328.
- Franklin, E. D. M., & Charru, F. (2009). Morphology and displacement of dunes in a closed-conduit flow. *Powder Technology*, 190(1), 247-251.
- Grigoriadis, D. G. E., Balaras, E., & Dimas, A. A. (2009). Large-eddy simulations of unidirectional water flow over dunes. *Journal of Geophysical Research: Earth Surface*, 114(F2).
- Gyr, A., & Schmid, A. (1997). Turbulent flows over smooth erodible sand beds in flumes. *Journal of hydraulic research*, 35(4), 525-544.

- Hanmaiahgari, P. R., & Balachandar, R. (2016). Turbulence characteristics of open channel flow over non-equilibrium 3-D mobile dunes. *Sādhanā*, 41(9), 1019-1037.
- Hino, M. (1968). Equilibrium-range spectra of sand waves formed by flowing water. *Journal of Fluid Mechanics*, 34(03), 565-573.
- Howard, A. D. (2007). Simulating the development of Martian highland landscapes through the interaction of impact cratering, fluvial erosion, and variable hydrologic forcing. *Geomorphology*, 91(3), 332-363.
- Jain, S. C., & Kennedy, J. F. (1974). The spectral evolution of sedimentary bed forms. *Journal of Fluid Mechanics*, 63(02), 301-314.
- Jerolmack, D. J., & Mohrig, D. (2005). A unified model for subaqueous bed form dynamics. *Water Resources Research*, 41(12).
- Jimenez, J. (2004). Turbulent flows over rough walls. *Annu. Rev. Fluid Mech.*, 36, 173-196.
- Kadota, A., & Nezu, I. (1999). Three-dimensional structure of space-time correlation on coherent vortices generated behind dune crest. *Journal of Hydraulic Research*, 37(1), 59-80.
- Kidanemariam, A. G., & Uhlmann, M. (2014). Direct numerical simulation of pattern formation in subaqueous sediment. *Journal of Fluid Mechanics*, 750, R2
- Kidanemariam, A. G., & Uhlmann, M. (2017). Formation of sediment patterns in channel flow: minimal unstable systems and their temporal evolution. *Journal of Fluid Mechanics*, (accepted arXiv:1702.06648)
- Kocurek, G., Ewing, R. C., & Mohrig, D. (2010). How do bedform patterns arise? New views on the role of bedform interactions within a set of boundary conditions. *Earth Surface Processes and Landforms*, 35(1), 51-63.
- Lapotre, M. G., Lamb, M. P., & McElroy, B. (2017). What sets the size of current ripples?. *Geology*, G38598-1.
- Maddux, T. B., Nelson, J. M., & McLean, S. R. (2003). Turbulent flow over three-dimensional dunes: 1. Free surface and flow response. *Journal of Geophysical Research: Earth Surface*, 108(F1).
- Meyer-Peter, E., & Müller, R. (1948). Formulas for bed-load transport. In *IAHSR 2nd meeting, Stockholm, appendix 2*. IAHR
- McLean, S. R., Nelson, J. M., & Wolfe, S. R. (1994). Turbulence structure over two-dimensional bed forms: Implications for sediment transport. *Journal of Geophysical Research: Oceans*, 99(C6), 12729-12747.
- Nelson, J. M., McLean, S. R., & Wolfe, S. R. (1993). Mean flow and turbulence fields over two-dimensional bed forms. *Water Resources Research*, 29(12), 3935-3953.
- Nelson, J. M., & Smith, J. D. (1989). Mechanics of flow over ripples and dunes. *Journal of Geophysical Research: Oceans*, 94(C6), 8146-8162.
- Nikora, V., Goring, D., McEwan, I., & Griffiths, G. (2001). Spatially averaged open-channel flow over rough bed. *Journal of Hydraulic Engineering*, 127(2), 123-133.
- Nikora, V. I., Sukhodolov, A. N., & Rowinski, P. M. (1997). Statistical sand wave dynamics in one-directional water flows. *Journal of Fluid Mechanics*, 351, 17-39.

- Nikuradse, J. (1933). Gesetzmäßigkeiten der turbulenten Strömung in glatten Rohren (Nachtrag). *Forschung auf dem Gebiet des Ingenieurwesens A*, 4(1), 44-44.
- Ouriemi, M., Aussillous, P., & Guazzelli, E. (2009a). Sediment dynamics. Part 1. Bed-load transport by laminar shearing flows. *Journal of Fluid Mechanics*, 636, 295-319.
- Ouriemi, M., Aussillous, P., & Guazzelli, E. (2009b). Sediment dynamics. Part 2. Dune formation in pipe flow. *Journal of Fluid Mechanics*, 636, 321-336.
- Papanicolaou, A. N., Diplas, P., Dancey, C. L., & Balakrishnan, M. (2001). Surface roughness effects in near-bed turbulence: Implications to sediment entrainment. *Journal of Engineering Mechanics*, 127(3), 211-218.
- Parker, G. (1975). Sediment inertia as cause of river antidunes. *Journal of the Hydraulics Division*, 101(2), 211-221.
- Pelletier, J. D. (2013). Deviations from self-similarity in barchan form and flux: The case of the Salton Sea dunes, California. *Journal of Geophysical Research: Earth Surface*, 118(4), 2406-2420.
- Perillo, M. M., Best, J. L., Yokokawa, M., Sekiguchi, T., Takagawa, T., & Garcia, M. H. (2014). A unified model for bedform development and equilibrium under unidirectional, oscillatory and combined-flows. *Sedimentology*, 61(7), 2063-2085.
- Omidyeganeh, M., & Piomelli, U. (2013). Large-eddy simulation of three-dimensional dunes in a steady, unidirectional flow. Part 1. Turbulence statistics. *Journal of Fluid Mechanics*, 721, 454.
- Raudkivi, A. J., & Witte, H. H. (1990). Development of bed features. *Journal of Hydraulic Engineering*, 116(9), 1063-1079.
- Ribberink, J. S., & Al-Salem, A. A. (1994). Sediment transport in oscillatory boundary layers in cases of rippled beds and sheet flow. *Journal of Geophysical Research: Oceans*, 99(C6), 12707-12727.
- Schindler, R. J., & Robert, A. (2005). Flow and turbulence structure across the ripple-dune transition: an experiment under mobile bed conditions. *Sedimentology*, 52(3), 627-649.
- Simons, D. B., Richardson, E. V., & Nordin Jr, C. F. (1960). Sedimentary structures generated by flow in alluvial channels.
- Spalart, P. R. (1988). Direct simulation of a turbulent boundary layer up to $R\theta = 1410$. *Journal of fluid mechanics*, 187, 61-98.
- Swanson, T., Mohrig, D., Kocurek, G., & Liang, M. (2016). A Surface Model for Aeolian Dune Topography. *Mathematical Geosciences*, 1-21.
- Venditti, J. G. (2003). *Initiation and development of sand dunes in river channels* (Doctoral dissertation, University of British Columbia).
- Venditti, J. G., & Bennett, S. J. (2000). Spectral analysis of turbulent flow and suspended sediment transport over fixed dunes. *Journal of Geophysical Research: Oceans*, 105(C9), 22035-22047.
- Yue, W., Lin, C. L., & Patel, V. C. (2005). Coherent structures in open-channel flows over a fixed dune. *Journal of fluids engineering*, 127(5), 858-864.
- Werner, B. T. (1995). Eolian dunes: computer simulations and attractor interpretation. *Geology*, 23(12), 1107-1110.

- Werner, B. T. (1999). Complexity in natural landform patterns. *Science*, 284(5411), 102-104.
- Werner, B. T. (2003). Modeling landforms as self-organized, hierarchical dynamical systems. *Prediction in geomorphology*, 133-150.
- Wong, M., & Parker, G. (2006). Reanalysis and correction of bed-load relation of Meyer-Peter and Müller using their own database. *Journal of Hydraulic Engineering*, 132(11), 1159-1168.
- Yalin, M. S. (2013). *Mechanics of sediment transport*. Pergamon press.
- Zedler, E. A., & Street, R. L. (2001). Large-eddy simulation of sediment transport: currents over ripples. *Journal of Hydraulic Engineering*, 127(6), 444-452.
- Zgheib, N., Fedele, J., Hoyal, D., Perillo, M., Balachandar, S. (2017). Direct numerical simulation of transverse ripples Part I. Pattern initiation and bedform interactions. *Submitted*

Table 1: Symbols, notation, and nomenclature definition. (* denotes dimensional quantity).

Variable/Notation	Symbol	Mathematical expression/definition
Scaling variables		
Mean flow depth (length scale)	H_f^*	-
Mean shear velocity (velocity scale)	U_τ^*	-
Time scale	T^*	H_f^*/U_τ^*
Flow-related variables		
3D velocity field	\mathbf{u}	
Perturbation pressure	p	
Numerical domain size (streamwise \times spanwise \times vertical)	$L_x \times L_y \times L_z$	-
Numerical resolution	$N_x \times N_y \times N_z$	-
Bulk velocity	U_b	$\frac{1}{L_y H_f} \int_0^{L_y} \int_0^{H_f} u \, dz \, dy$
Fluid density	ρ_f^*	-
Gravitational acceleration	g^*	-
Fluid kinematic viscosity	ν^*	-
Fluid dynamic viscosity	μ^*	-
Particle Reynolds number	Re_p	$\frac{1}{\nu^*} \sqrt{\frac{\rho_p^* - \rho_f^*}{\rho_f^*} g^* d_p^{*3}}$
Shear Reynolds number	Re_τ	$U_\tau^* H_f^* / \nu^*$
Bed-related variables		
Bed shear stress	τ^*	$\left(\frac{\mu^* U_\tau^*}{H_f^*} \right) \frac{\partial u}{\partial n}$
Shields number	Θ	$\tau^* / [(\rho_p^* - \rho_f^*) g^* d_p^*]$
Critical Shields number	Θ_{cr}	$\frac{1}{2} [0.22 Re_p^{-0.6} + 0.06 \exp(-17.77 Re_p^{-0.6})]$ $(Re_p/Re_\tau) c_1 (\Theta - \Theta_{cr})^{c_2}$
Volumetric flux of sediment per unit width ^x	q	
Bed volume fraction	φ	$1 - \text{porosity}$
Diffusion coefficient	ϵ	-
Bed elevation (w.r.t mean)	h	-
Mean bed height	\bar{h}	-
Sediment diameter	d_p^*	-
Sediment density	ρ_p^*	-
Notation		
Unit vector	e	
x, y, z , bed-tangent, bed-normal components of quantity ■	$\{■_x, ■_y, ■_z, ■_t, ■_n\}$	
Time average of quantity ■	$\langle ■ \rangle$	$\frac{1}{T} \int_{t_1}^{t_1+\psi} ■ \, dt$
Spanwise average of quantity ■	$\overline{■}$	$\frac{1}{L_y} \int_0^{L_y} ■ \, dy$
Stream and span average of quantity ■	$\overline{\overline{■}}$	$\frac{1}{L_x L_y} \int_0^{L_y} \int_0^{L_x} ■ \, dx \, dy$

Table 2. List of simulations presented in Paper I and shown here for completeness. d_p^* , ρ_p^* , and ρ_f^* are the sediment diameter, sediment density, and fluid density respectively. Re_p is the sediment Reynolds number. Θ_{cr} is the critical Shields number and Θ is the Shields number imposed by the flow. Re_τ is the shear Reynolds number based on the bed shear velocity U_τ^* and flow depth H_f^* . U_b^* and H_b^* are the bulk velocity and sediment thickness, respectively. L_x , L_y , and L_z represent the computational domain length, width, and height, respectively. N_x , N_y , and N_z correspond to the number of grid points along the streamwise, spanwise, and vertical directions, respectively.

Simulation number	d_p^* (μm)	ρ_p^* (g/cm^3)	ρ_f^* (g/cm^3)	Re_p	Θ_{cr}	Θ	Θ/Θ_{cr}	Re_τ	U_τ^* (cm/s)	U_b^* (cm/s)	H_f^* (cm)	H_b^* (mm)	$L_x \times L_y \times L_z$	$N_x \times N_y \times N_z$
S1	250	1.57	1.015	9.347	0.029	0.109	3.76	180	1.237	19.32	1.455	0.728	$12 \times 4 \times 1.05$	$288 \times 96 \times 301$
S2	150	1.57	1.015	4.344	0.046	0.182	4.00	180	1.237	19.32	1.455	0.728	$12 \times 4 \times 1.05$	$288 \times 96 \times 301$
S3	50	1.57	1.015	0.836	0.122	0.547	4.47	180	1.237	19.32	1.455	0.728	$12 \times 4 \times 1.05$	$288 \times 96 \times 301$
S4	250	1.57	1.015	9.347	0.029	0.055	1.88	180	0.874	13.65	2.058	1.03	$12 \times 4 \times 1.05$	$288 \times 96 \times 301$
S5	150	1.57	1.015	4.344	0.046	0.091	2.00	180	0.874	13.65	2.058	1.03	$12 \times 4 \times 1.05$	$288 \times 96 \times 301$
S6	50	1.57	1.015	0.836	0.122	0.274	2.23	180	0.874	13.65	2.058	1.03	$12 \times 4 \times 1.05$	$288 \times 96 \times 301$

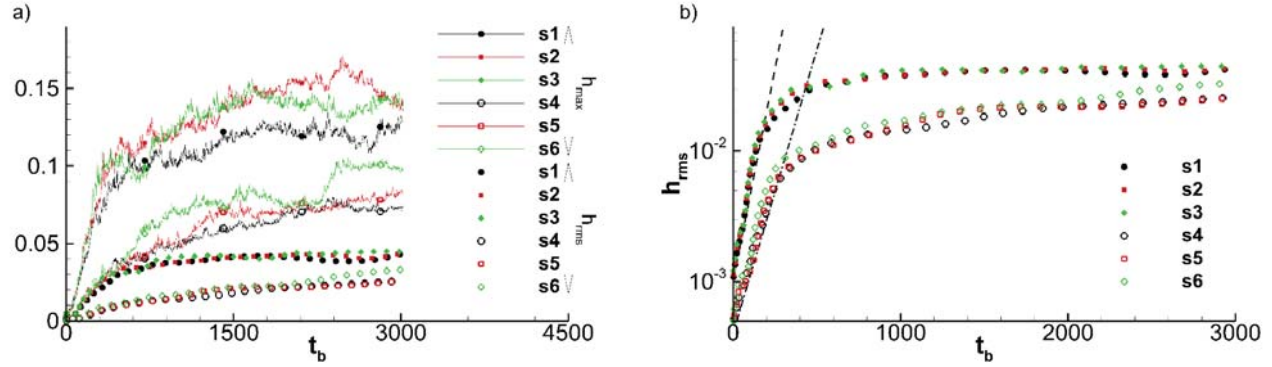


Figure 1. (a) Temporal evolution of the maximum and rms bed height fluctuation. (b) Same as (a) but with linear-log scale to show the exponential growth of h_{rms} . The exponential growth is observed in approximately the first 200 bulk time units. The dashed and dash dot lines correspond to exponential fits of $h_{rms} = 10^{-3}\exp(0.015t_b)$ and $h_{rms} = 4 \times 10^{-4}\exp(0.01t_b)$, respectively.

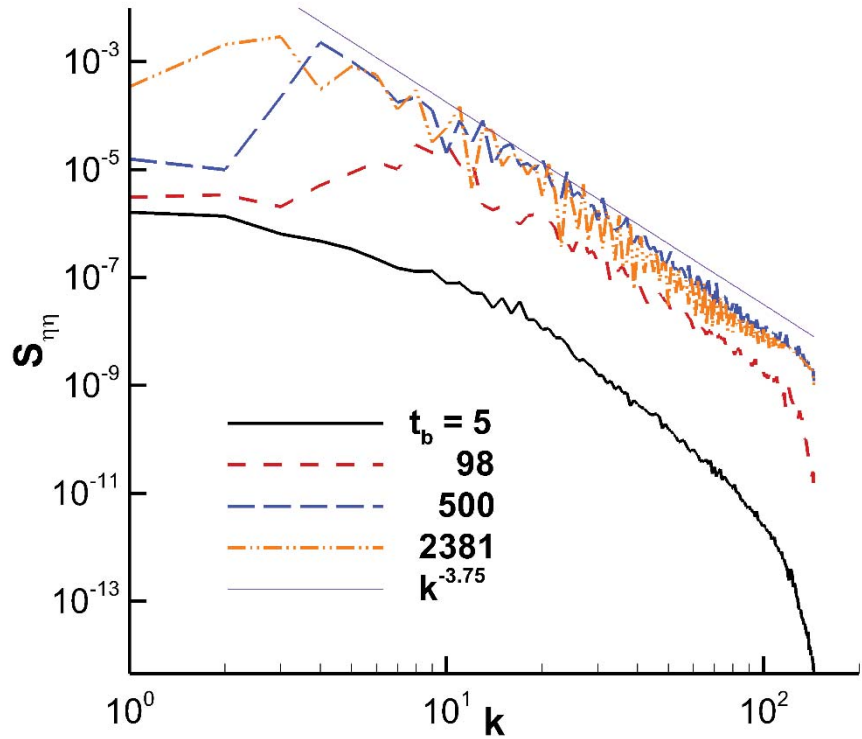


Figure 2. Wave number spectra from S2 at five time instances. For $t_b > 500$, we observe a decay rate of -3.75 (thin solid purple line)

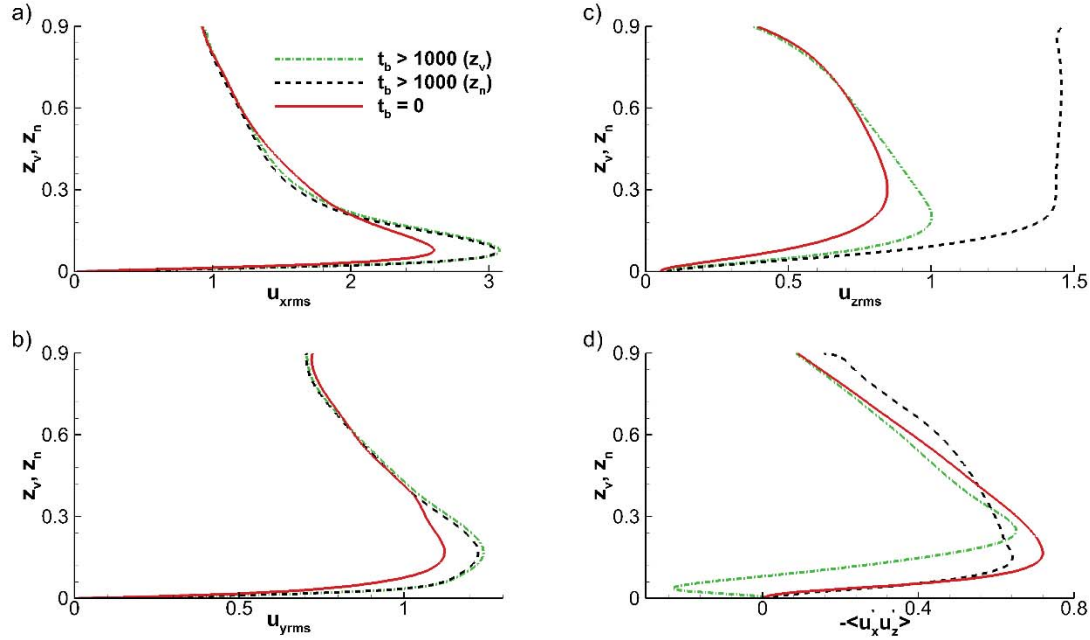


Figure 3. rms velocity fluctuations over the entire computational domain vs distance from the bed (z_v, z_n) for the a) streamwise b) spanwise, and c) and vertical components of velocity for case S2 at the start of the simulation (solid red line) and beyond $t_b = 1000$ (black dashed & green dash-dotted lines). d) same as other frames, but for Reynolds stress $-\langle u'_x u'_z \rangle$.

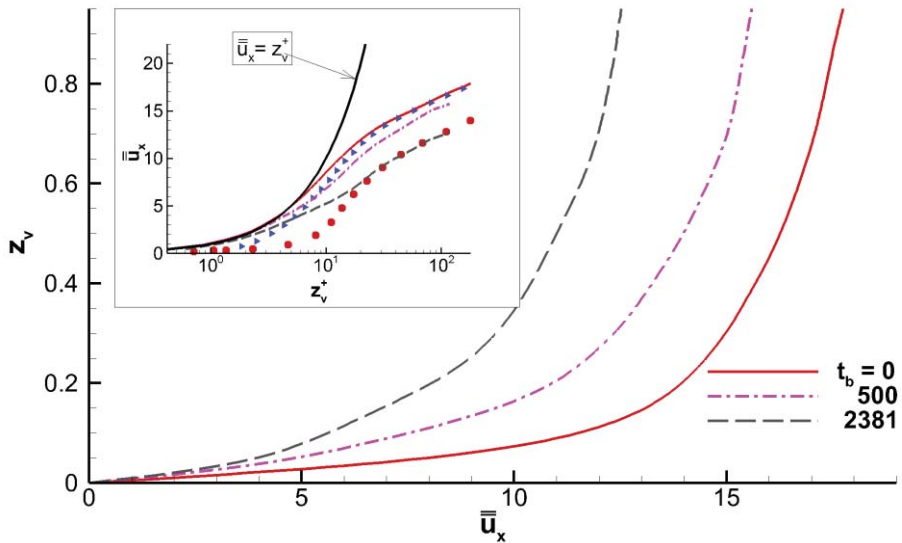


Figure 4. Stream and span-averaged x -component of velocity versus vertical distance from the bed z_v at different instances for case S2. (Inset) same as main figure but for wall units z_v^+ on a log-linear plot. The symbols correspond to velocity profile from an actual rough wall simulation (Chan-Braun *et al.* 2011). Note that the axes in the main figure and inset are inverted.

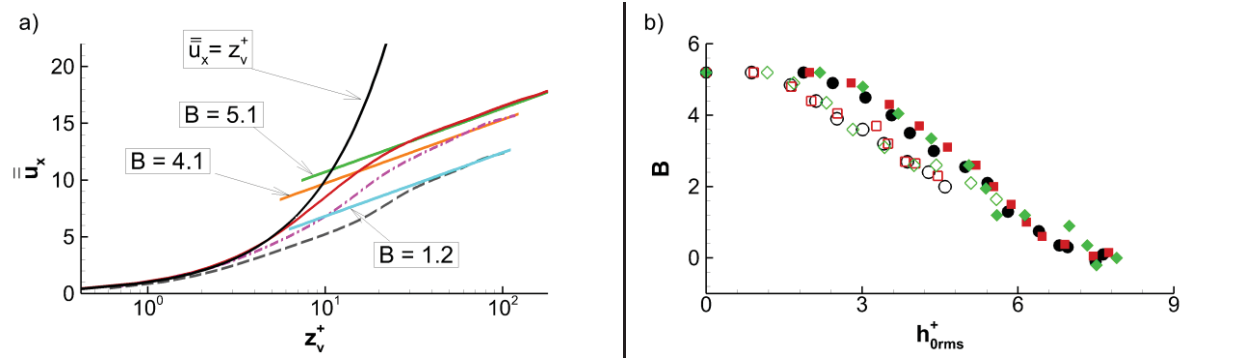


Figure 5. Second coefficient in the logarithmic law-of-the-wall vs rms bed height in wall units. (inset) Same as main figure except that U_τ^* is used as velocity scale instead of $\bar{u}_\tau^*(t)$.

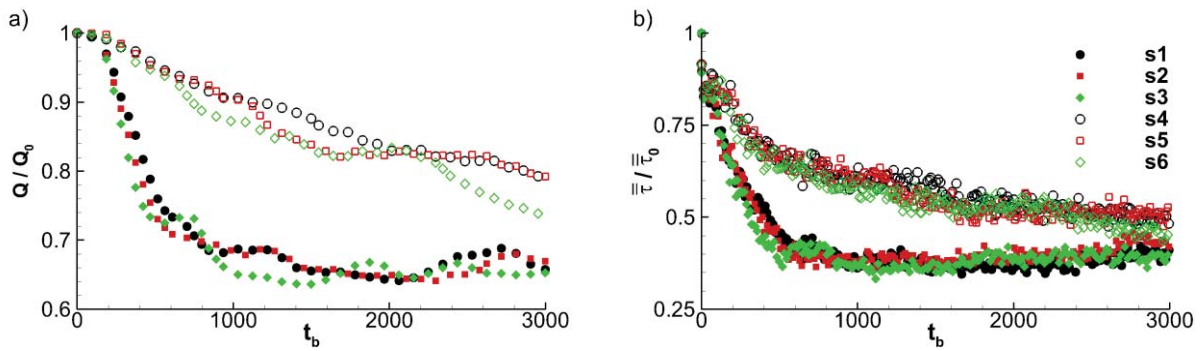


Figure 6. a) Flow rate Q normalized by the initial flow rate Q_0 at the start of the simulation. b) Stream and span-averaged shear stress $\bar{\tau}$ normalized by the stream and span-averaged shear stress $\bar{\tau}_0$ of the initially flattened bed at the start of the simulation.

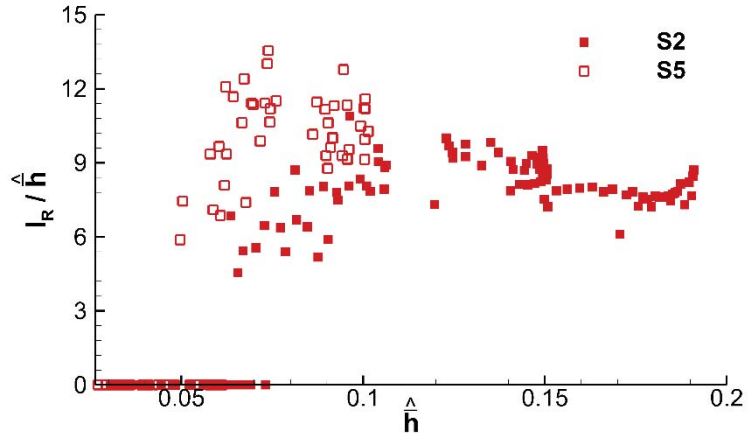


Figure 7. Streamwise extent (beyond the crest) of the recirculation region versus span-averaged crest height, measured from crest to subsequent trough. Results from **S2** for $t_b > 1000$ and **S5** for $t_b > 2500$. No recirculation is detected for values of $\hat{h} < 0.05$.

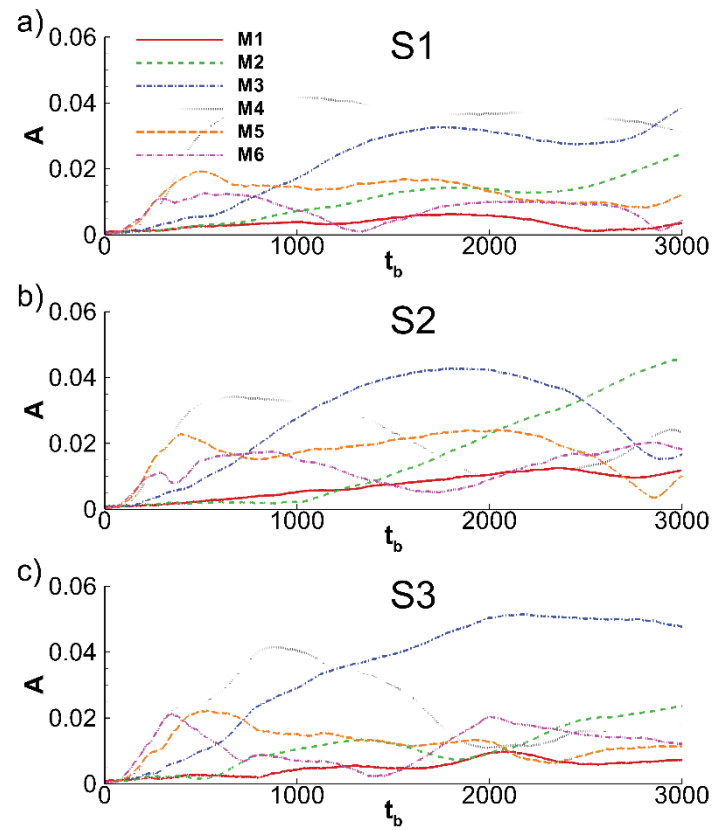


Figure 8. Temporal evolution of the amplitude of the first 6 Fourier modes.

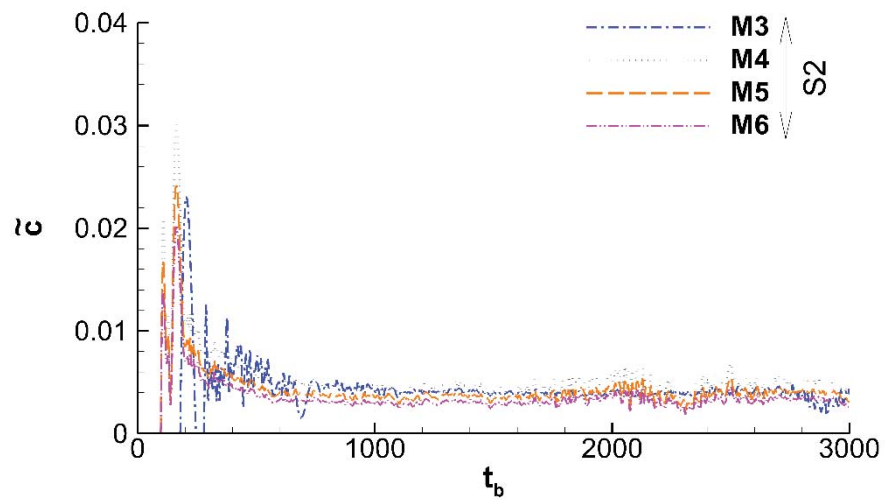


Figure 9. Temporal evolution of the phase speed \tilde{c} for modes, M3 through M6, for case S2.

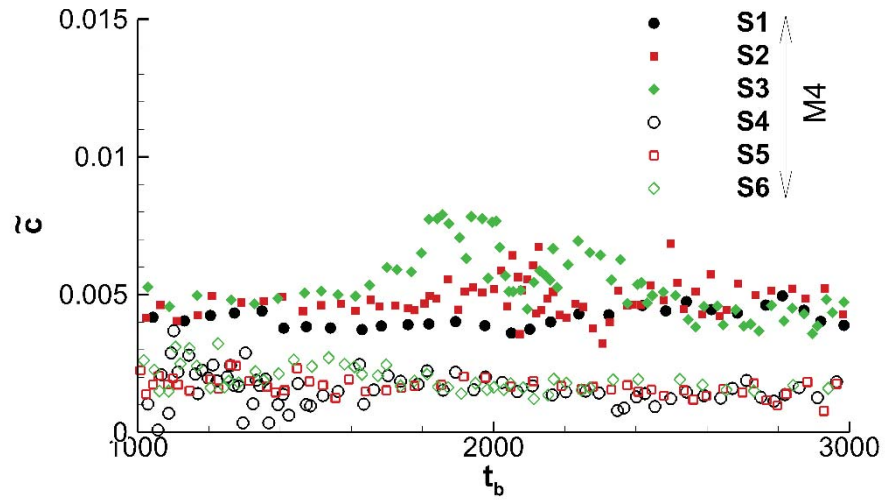


Figure 10. Temporal evolution of the phase speed \tilde{c} for the 4th mode M4 from the six cases, S1 through S6.

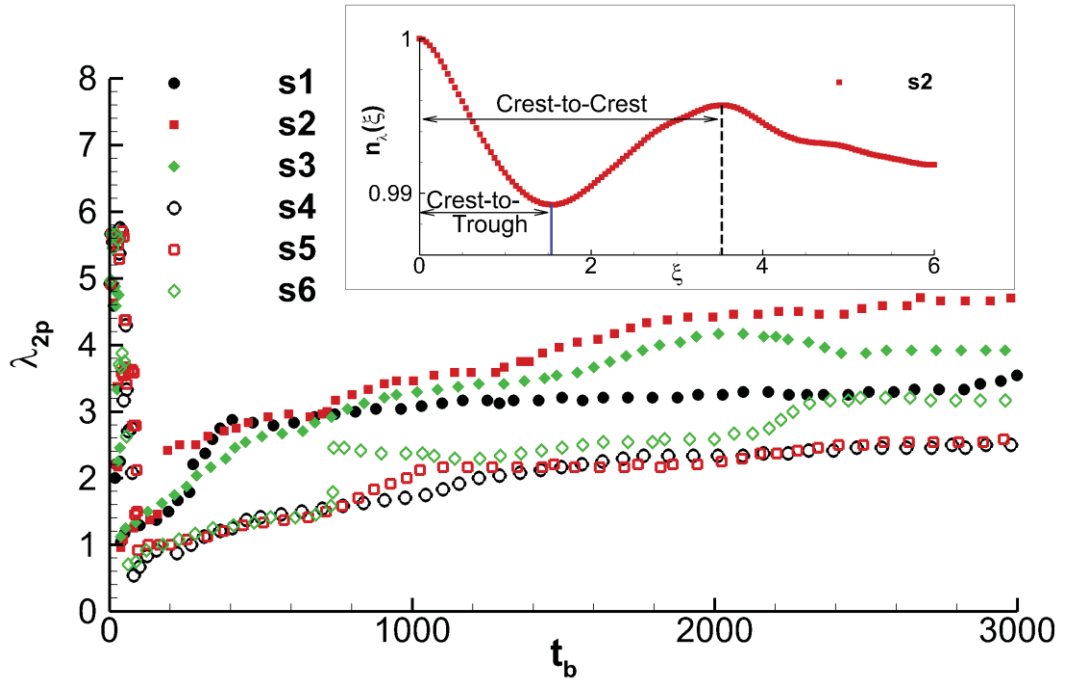


Figure 11. Dominant bed height wavelength λ_{2p} vs time. Inset: two-point correlation function versus separation ξ showing the dominant crest-to-trough and crest-to-crest separation at $t_b = 1220$ for case S2.

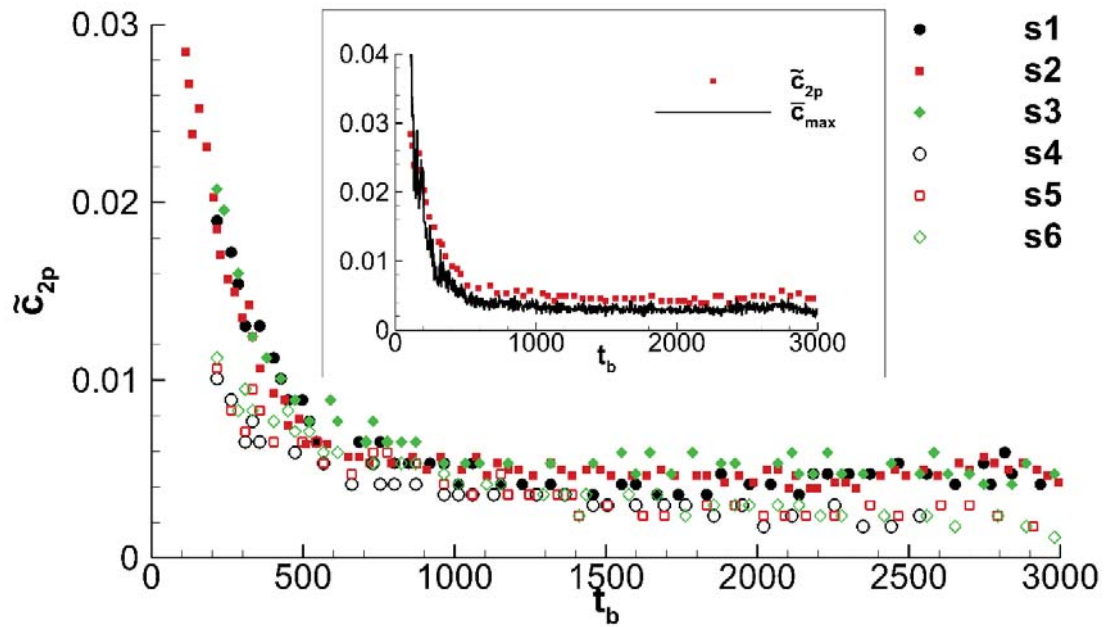


Figure 12. Temporal evolution of \tilde{c}_{2p} , the bed velocity normalized by the bulk velocity U_b^* , inset: temporal evolution of \tilde{c}_{2p} and \bar{c}_{max} for case S2 .

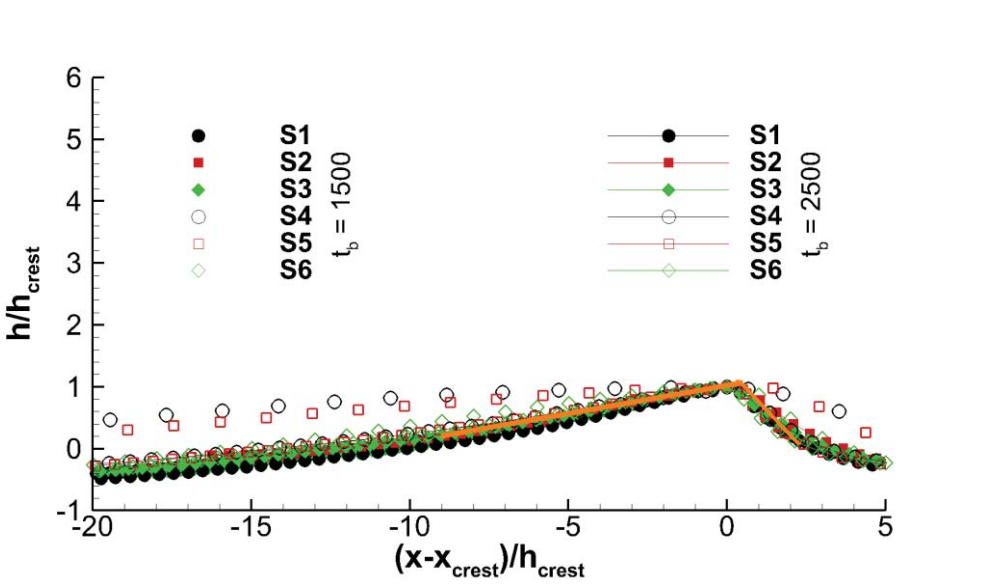


Figure 13. Cross-sectional shape of the largest ripple in the centre plane ($y = 2$) for all S^* cases in Table 2 at $t_b = 1500$ (symbols) and $t_b = 2500$ (symbols + lines). The ripple height and length have been scaled by the respective crest height (h_{crest}). Additionally, all the ripples have been translated along the x -axis for comparison. The orange segments provide an estimate of the slope at the stoss and lee sides of the ripples, which approximately correspond to an angle of 5° and 30° , respectively.

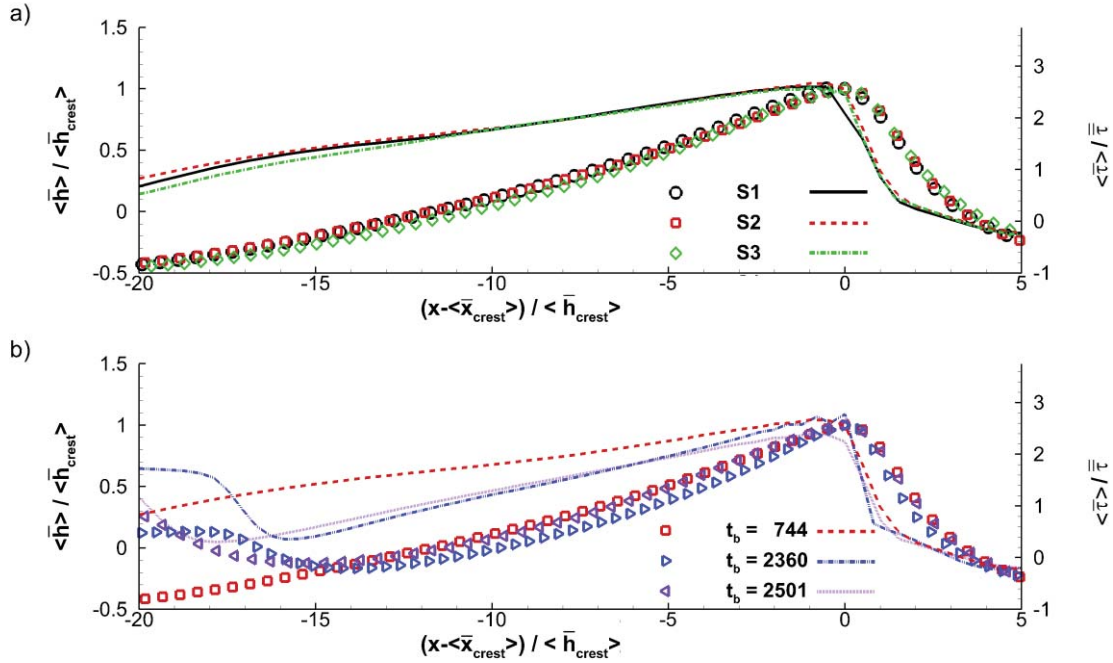


Figure 14. a) The symbols correspond to the span-averaged cross-sectional shape of a span invariant, isolated ripple at $t_b = 744$ from $S1$, $S2$, and $S3$ scaled by the span-average crest height. The lines correspond to the span and time-averaged shear stress for each ripple scaled by the instantaneous span and stream averaged shear stress. b) same as (a) but for the same ripple from $S2$ at different times. The presence of an upstream neighbour modifies the shear stress on the stoss side and eventually leads the cross-sectional shape to a deviate from the self-similar profile.

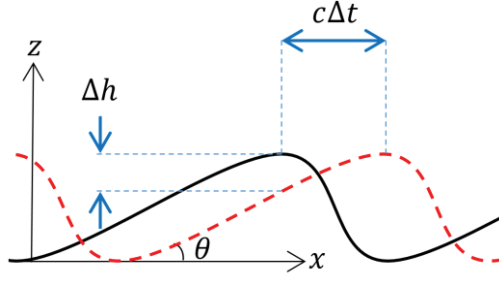


Figure 15. Schematic for a self-similar ripple at time t (solid black line) and $t + \Delta t$ (dashed red line) undergoing pure translational motion, with no growth or decay, at a velocity c .

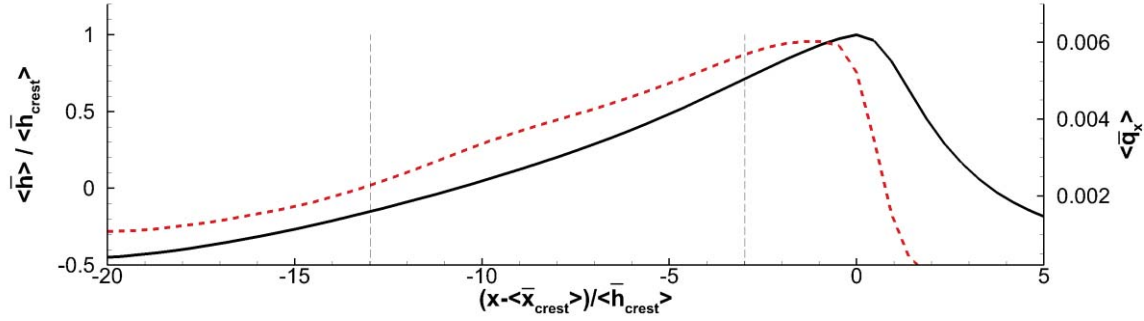


Figure 16. Cross-sectional shape (black solid line) of a span and time averaged self-similar ripple from S3 at $t_b = 2009$ along with the span and time averaged streamwise component of bedload flux (red dashed line). The x -axis and the bed height variation are normalized by the crest height.

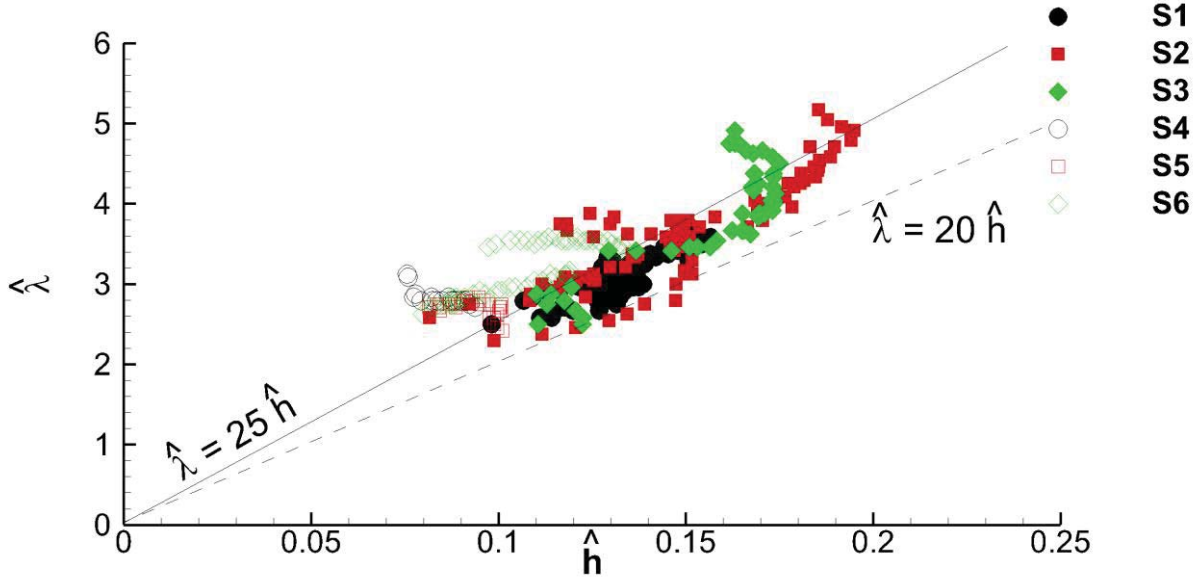


Figure 17. Wavelength vs wave height for self-similar ripples from cases S1 through S6.

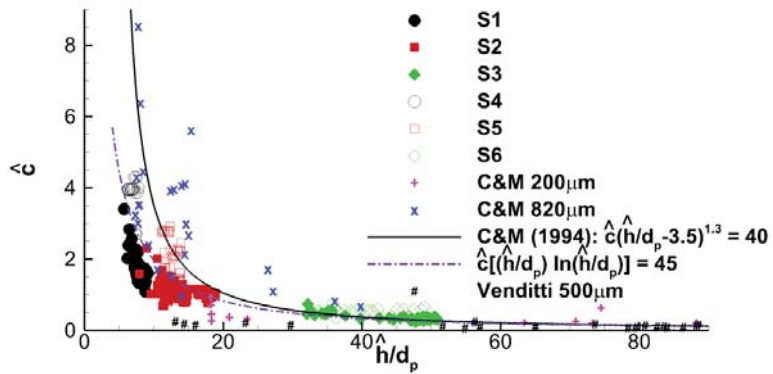


Figure 18. Ripple speed vs ripple height for self-similar ripples for cases S1 through S6. Present data is compared with the empirical fit (black solid line) and laboratory measurements ($\{+\}, \times\}$ for $\{200, 820\}\mu\text{m}$ sand particle, respectively) of Coleman & Melville (1994) as well as laboratory measurement (#) of Venditti (2003). The dashed dotted line $\hat{c} \frac{\hat{h}}{d_p} \ln \left(\frac{\hat{h}}{d_p} \right) = 45$ provides a better fit to the present data.

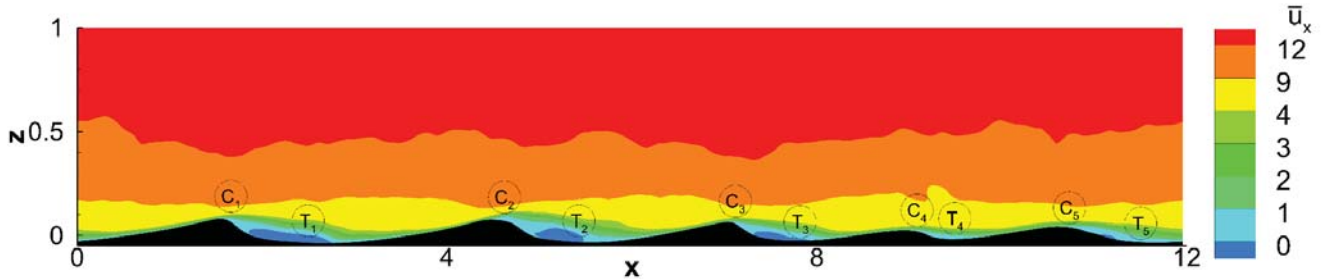


Figure 19. Span averaged bed and streamwise component of velocity for case S2 at $t_b = 515$ when the bed has become nearly span invariant. The bed consists of five ripples and troughs marked as C_* and T_* , respectively. Note that because of periodicity, T_5 is also the trough upstream of C_1 .

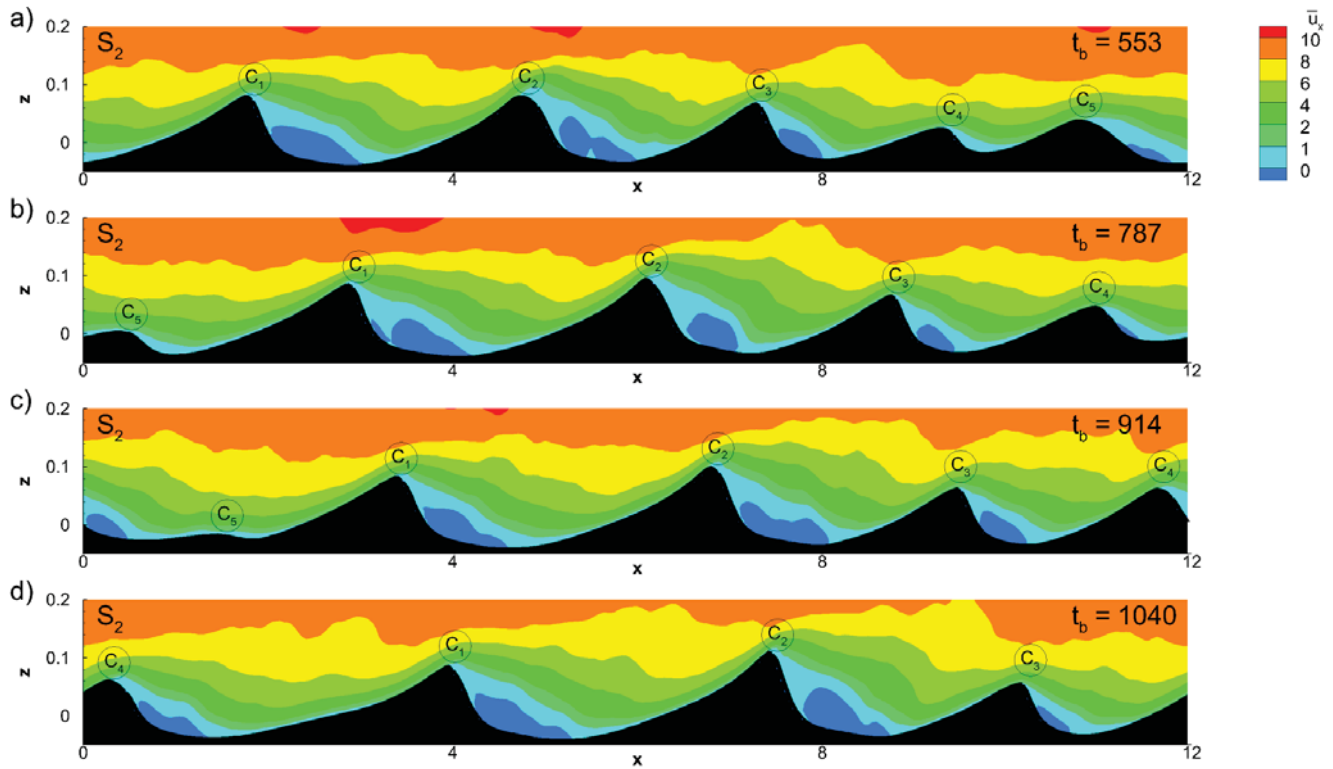


Figure 20. Time series of the spanwise-averaged bed and streamwise component of velocity from case S2 showing wave coarsening through remote interaction. The diminished ripple C_5 in frame c goes on to merge with the downstream ripple C_1 .

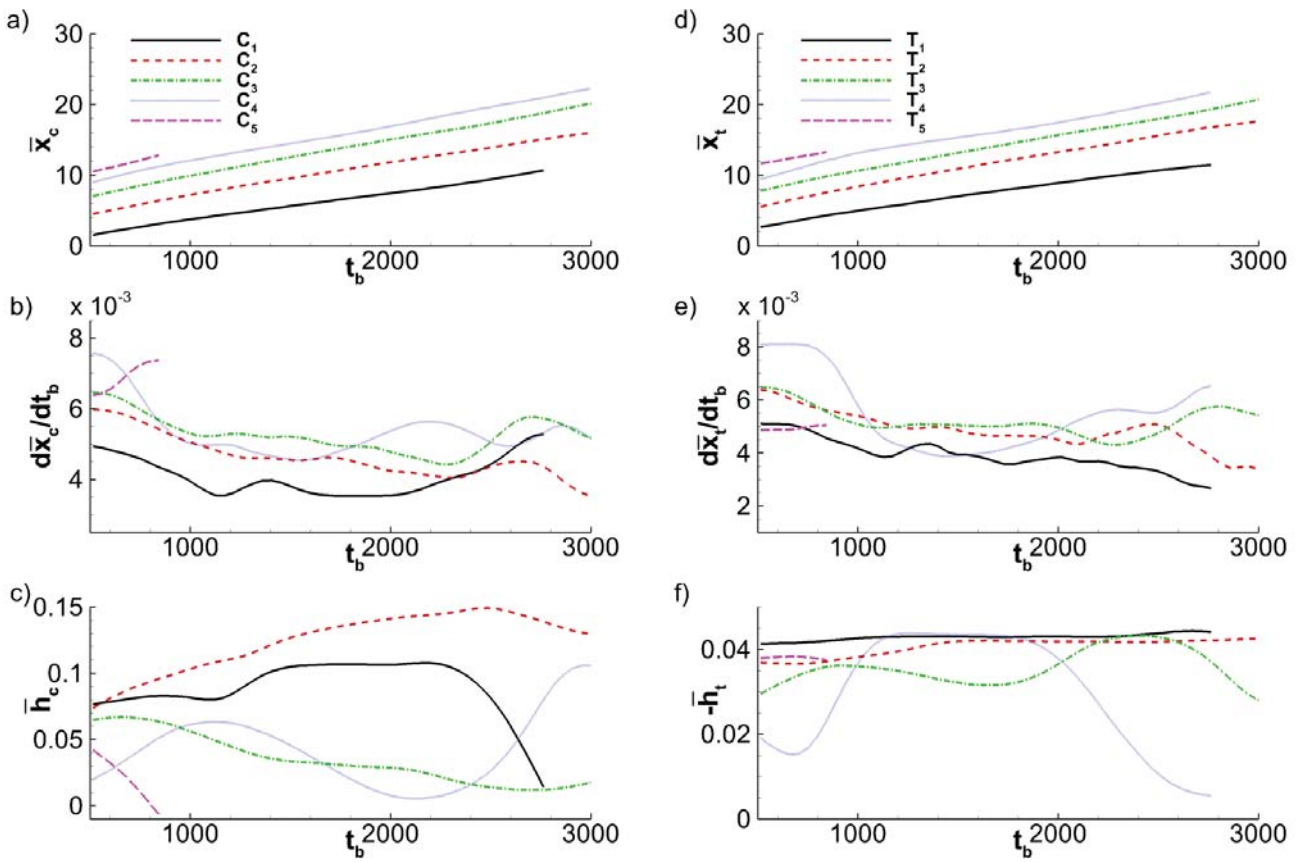


Figure 21. Temporal evolution of spanwise-averaged quantities from case S2 of a) crest position, b) crest velocity, c) above-mean crest elevation, d) trough position, e) trough velocity, and f) below-mean trough depth.